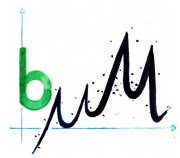# Carbon and Energy Exchange in a Tropical Dry Forest in Costa Rica with regard to El Niño-Southern Oscillation Dynamics

Master thesis in Geoecology
Elena Loos
Matricle number: 1328639

supervised by
Prof. Dr. Christoph Thomas
Dr. Wolfgang Babel

University of Bayreuth
Micrometeorology group

January 27, 2020

Contents

List of Figures

List of Tables

List of Symbols and Abbreviations

Symbol	Description	Physical unit
ACG	Area de Conservation Guanacaste	
Bo	Bowen ratio	-
dry	Dry season	
EC	Eddy covariance	
ENSO	El Niño-Southern Oscillation	
ET	Evapotranspiration	$kg_{H_2O}\,m^{-2}\,d^{-1}$, mm
EWUE	Ecosystem water use efficiency	$g_C\,kg_{H_2O}^{-1}$
FCO$_2$	Carbon dioxide flux	$\mu mol_C\,m^{-2}\,s^{-1}$
GPP	Gross primary production	$g_C\,m^{-2}\,d^{-1}$, $g_C\,m^{-2}\,yr^{-1}$
HEY	Hydroecological year	
IWUE	Inherent water use efficiency	$g_C\,hPa\,kg_{H_2O}^{-1}$
K$_{net}$	Net shortwave radiation	$W\,m^{-2}$
K↑	reflected shortwave radiation	$W\,m^{-2}$
LUE	Light use efficiency	$mol_C\,mol_{photon}^{-1}$
NDVI	Normalized difference vegetation index	-
NEE	Net ecosystem exchange	$g_C\,m^{-2}\,d^{-1}$, $g_C\,m^{-2}\,yr^{-1}$
PPFD	Photosynthetic photon flux density	$\mu mol_{photon}\,m^{-2}\,s^{-1}$
QAQC	Quality assessment and quality control	
Q$_E$	Latent heat flux	$W\,m^{-2}$
Q$_H$	Sensible heat flux	$W\,m^{-2}$
R$_{eco}$	Ecosystem respiration	$g_C\,m^{-2}\,d^{-1}$, $g_C\,m^{-2}\,yr^{-1}$
R$_g$	Global radiation/incoming shortwave radiation	$W\,m^{-2}$
R$_{net}$	Net radiation	$W\,m^{-2}$
RWUE	Respiration water use efficiency	$g_C\,kg_{H_2O}^{-1}$
sdry	Summer dry season/veranillo	
SRNP	Santa Rosa National Park	

Symbol	Description	Physical unit
SST	Sea surface temperature	°C
τ	Momentum flux	$\mathrm{m^2\,s^{-2}}$
TDF	Tropical dry forest	
trans	Transition period	
u_*	Friction velocity	$\mathrm{m\,s^{-1}}$
VPD	Vapor pressure deficit	hPa
wet	Wet/rainy season	
WUE	Water use efficiency	$\mathrm{g_C\,kg_{H_2O}^{-1}}$

Abstract

Tropical Dry Forests (TDFs) are important tropical ecosystems, accounting for a quarter of the forested area in the tropics and a significant impact on the global terrestrial net carbon (C) sink. Amount and distribution of annual precipitation are the main drivers for changes in the carbon balance of TDFs. As El Niño-Southern Oscillation (ENSO) events largely influence interannual precipitation patterns, the carbon balance of the TDF in the study region is altered by ENSO impacts. Projections show effects of global warming until 2100 similar to dry and warm summers which occur currently during El Nino events, thus they provide the possibility to analyze future reactions of the TDF ecosystems to climate change.

The objectives of this study were (1) to quantify the carbon fluxes net ecosystem exchange (NEE), gross primary production (GPP) and ecosystem respiration (R_{eco}), the energy fluxes latent heat flux (Q_E), sensible heat flux (Q_H) and the momentum flux, analyzing them for the wet and dry season individually by delineating functional seasonality and (2) to evaluate effects of ENSO events on the component carbon fluxes and the net carbon balance.

To achieve this, carbon, energy, and momentum fluxes were measured with the eddy covariance method at the Environmental Monitoring Super Site in a tropical dry forest in northwestern Costa Rica. The monitoring site is part of the research network Tropi-Dry. The work is a collaboration with the research group from Prof. Dr. G. A. Sánchez-Azofeifa at the University of Alberta, Canada. Additionally, functional seasons were defined using the normalized difference vegetation index from satellite images and ENSO events were classified using sea surface temperatures. Fluxes were analyzed and compared for the individual functional seasons and ENSO events.

The results showed that the ecosystem is a net sink throughout the year with daily rates of net carbon uptake which were about $3\,g_C\,m^{-2}\,d^{-1}$ higher during the wet season than during the dry season. Only in years with an El Niño event, which lead to higher temperatures and decreased precipitation, and in years with and La Niña event, which lead to lower temperatures and increased precipitation, the ecosystem turned into a net carbon source during the dry season. Most negative annual sums of NEE, which indicate net carbon uptake, were found for years with neutral ENSO conditions. Both La Niña and El Niño years reduce the strength of the net carbon sink, the strong El Niño event in 2015 reducing the sink by almost two thirds (NEE of $-351\,g_C\,m^{-2}\,yr^{-1}$ in 2015 compared to $-889\,g_C\,m^{-2}\,yr^{-1}$ during neutral conditions).

This indicates that the TDF is an ecosystem which is highly adapted to its climatic conditions, achieving greatest annual net carbon uptakes during years with mean precipitation amounts. The

results also indicate that the ecosystem is highly vulnerable to climate change. Under El Niño-like conditions, which could be the normal state in a future climate, net carbon uptake would be greatly reduced.

Zusammenfassung

Tropischer Trockenwald (TDF, tropical dry forest) ist ein wichtiger Bestandteil der tropischen Ökosysteme. Flächenmäßig nimmt tropischer Trockenwald den etwa ein viertel der Waldfläche in den Tropen ein und auch für die globale terrestrische Netto-Kohlenstoffaufnahme ist er ein wichtiger Faktor. Die Haupteinflussfaktoren für die Kohlenstoffbilanz in TDFs sind die Menge an Niederschlag und die Verteilung über das Jahr. Da El Niño-Southern Oscillation (ENSO) Ereignisse Verteilung und Menge des Niederschlags im Untersuchungsgebiet beeinflussen, wird die Kohlenstoffbilanz des TDFs durch ENSO Ereignisse verändert. Und da Vorhersagen zeigen, dass der Klimawandel bis 2100 im Untersuchungsgebiet ähnliche Auswirkungen haben könnte wie warme und trockene El Niño Jahre, bieten diese die Möglichkeit, die Auswirkungen des Klimawandels auf das Ökosystem tropischer Trockenwald zu untersuchen.

Ziel dieser Arbeit war es, (1) die Kohlenstoffflüsse Netto-Ökosystemaustausch (NEE, net ecosystem exchange), Bruttoprimärproduktion (GPP, gross primary production) und Ökosystematmung (R_{eco}, ecosystem respiration), die Energieflüsse latente Wärme (Q_E) und fühlbare Wärme (Q_H) und den Impulsfluss zu quantifizieren. Außerdem wurden funktionelle Jahreszeiten definiert und die Flüsse getrennt nach den Jahreszeiten analysiert. Und (2) zu untersuchen, wie sich Kohlenstoff- und Energieflüsse und der Impulsfluss bei ENSO Ereignissen verändern.

Um diese Ziele zu erreichen wurden auf der Environmental Monitoring Super Site im Santa Rosa National Park in Costa Rica die Kohlenstoff- und Energieflüsse und der Impulsfluss mit der Eddy-Kovarianz-Methode gemessen. Die Messstelle ist Teil des Forschungsnetzwerks Tropi-Dry. Die Arbeit ist eine Zusammenarbeit mit der Forschergruppe von Prof. Dr. G. A. Sánchez-Azofeifa an der Universität von Alberta, Kanada. Der normalisierte differenzierte Vegetationsindex (NDVI, normalized difference vegetation index), der aus Satellitenbildern bestimmt wird, wurde genutzt, um die unterschiedlichen funktionellen Jahreszeiten zu definieren. Außerdem wurden ENSO Ereignisse für die Jahre des Messzeitraums anhand von Anomalien in den Oberflächenwassertemperaturen (SST, sea surface temperature) im Pazifik identifiziert. Die Kohlenstoff- und Energieflüsse wurden dann für die unterschiedlichen funktionellen Jahreszeiten und ENSO Ereignisse untersucht und miteinander verglichen.

Die Ergebnisse der Studie zeigten, dass das Ökosystem das gesamte Jahr über eine Netto-Kohlenstoffsenke war. Die tägliche Netto-Kohlenstoffaufnahme war in der Regenzeit um etwa $3\,\mathrm{g_C}\,\mathrm{m}^{-2}\,\mathrm{d}^{-1}$ höher als in der Trockenzeit. Nur in El Niño-Jahren, die trockener und wärmer sind und La Niña-Jahren, die feuchter und kühler sind als Jahre ohne ENSO Ereignis, wurde der

tropische Trockenwald in der Trockenzeit zu einer Kohlenstoffquelle. Die Jahressummen des NEE waren für das Jahr mit neutralen ENSO Bedingungen am negativsten, was eine starke Kohlenstoff-senke bedeutet. In El Niño- und La Niña-Jahren war die Stärke der Kohlenstoffsenke reduziert, im Falle des starken El Niño-Jahres 2015 wurde die Kohlenstoffsenke sogar um fast zwei Drittel im Vergleich zum neutralen ENSO-Jahr verringert (NEE von $-351\,\mathrm{g_C\,m^{-2}\,yr^{-1}}$ für 2015 verglichen mit $-889\,\mathrm{g_C\,m^{-2}\,yr^{-1}}$ für 2013 mit neutralen ENSO Bedingungen).

Dies deutet darauf hin, dass das Ökosystem sehr gut an dort herrschenden Bedingungen ange-passt ist und die höchste Netto-Kohlenstoffaufnahme bei mittleren Niederschlagsmengen geschieht. Weder höhere noch geringere Niederschläge erhöhen die Netto-Kohlenstoffaufnahme. Die Ergebnis-se deuten auch darauf hin, dass der tropische Trockenwald sehr empfindlich auf den Klimawandel reagieren könnte. El Niño-ähnliche Bedingungen, die in Zukunft den Normalzustand darstellen könnten, verringern die Netto-Kohlenstoffaufnahme erheblich.

1. Introduction

Forests still cover about 31% of the terrestrial surface, although heavy deforestation has decreased the world's forested area. Compared to what the natural extent would be, the forested area is diminished by two thirds in temperate and boreal zones and by one quarter in tropical zones. Over the last two and a half decades, the area still decreased by 3% (FAO, 2015; Keenan et al., 2015; Pan et al., 2013).

Forests are most important for the global C cycle. Through photosynthesis plants assimilate carbon (C) from atmospheric carbon dioxide (CO_2) and thereby remove CO_2 from the atmosphere. On the scale of ecosystems, the flux of carbon assimilation is called gross primary production (GPP). About 48% of the global terrestrial GPP are found to come from all forests and 34% from only tropical forests (Beer et al., 2010). However, for the net carbon uptake, emissions from ecosystem respiration (R_{eco}), wildfires (C_{fire}) and land use change (tropical regrowth and deforestation, F_{LUC}) have to be taken into account. Taking emissions into account results in net biome production ($NBP = GPP - R_{eco} - C_{fire} - F_{LUC}$). Regarding NBP, there is still great uncertainty about its magnitude in tropical forests. Pan et al. (2011) found that, although NBP is increased by regrowing tropical forest, heavy deforestation in the tropics decreases NBP strongly, resulting in the entire tropical forest being almost carbon neutral. Afforestation efforts could therefore help mitigate climate change (Becknell et al., 2012; Pan et al., 2011), counteracting human induced CO_2 emissions (Malhi et al., 1999). Ahlström et al. (2015) on the contrary found that tropical forests account for the largest part of global mean NBP (24 to 26% for different models). On the other hand, several authors agree in their findings that semi-arid ecosystems are the main cause for trend (51%) and interannual variability (IAV, 39%) of the global NBP (Ahlström et al., 2015; Poulter et al., 2014). Especially in semi-arid ecosystems negative and positive anomalies in GPP correlate strongly with unusually warm and dry or cool and wet periods respectively (Huang et al., 2016).

In the tropics as defined after the Holdridge Life Zone system, 49% of the land surface is covered by forest. The largest part of that forest is tropical moist forest with 47%, followed by troical wet and rain forest with 29% and tropical dry forest (TDF) with 24%. North and Central America contain 39% and Costa Rica contains 0.4% of all the tropical dry forest in the Americas (Brown and Lugo, 1982; Portillo-Quintero and Sánchez-Azofeifa, 2009).

According to Miles et al. (2006), the estimated remaining area of TDF was about $1\,048\,700\,km^2$, of which 54.2% were located in South America and 12.5% in North and Central America. Hoekstra

et al. (2005) found that tropical dry forests suffer from the greatest habitat loss and only moderate protection when compared to other ecosystems. According to Ewel (1999), life zones of dry forest after Holdridge are well suited for agriculture. On the one hand they are not too wet, which reduces leaching of minerals and suppresses insect pests as the dry seasons have a similar sterilizing effect as northern winters. On the other hand they are also not too dry, rainfall and pET deviating not significantly, that only moderate irrigation is needed (Janzen, 1986). This leads to high deforestation rates, highly fragmented ecosystems, and dense population (Tosi and Voertman, 1964).

As the boundaries of tropical dry forests to other vegetation types such as savannas, woodlands, and wet forests are blurred they are difficult to characterize. A wide range of definitions exists, mostly depending on mean annual temperature and precipitation. For example, Holdridge's (1967) life zones define TDFs as having a mean annual temperature of $17\,°C$ or higher, a mean annual rainfall of 500 to 2000 mm, and an annual ratio of potential evapotranspiration (pET) to precipitation exceeding unity. According to Sánchez-Azofeifa et al. (2005), tropical dry forests are dominated by drought deciduous vegetation and characterized by a mean annual temperature of $25\,°C$, precipitation ranging between 700 and 2000 mm per year, and a dry season with less than $100\,\mathrm{mm\,mon^{-1}}$ of three or more months.

Together with deforestation, climate change is a major threat to TDFs in Northern and Central America (Miles et al., 2006). Karmalkar et al. (2011) found that due to climate change temperatures could increase by 3 to $4\,°C$ and precipitation could decrease by 16 to $25\,\%$ at the Pacific coast of Central America until 2100. The climate in Central America is strongly influenced by El Niño-Southern Oscillation (ENSO) dynamics. Model projections showed that climate change could have similar impacts as warm El Niñno events, increasing temperatures and decreasing precipitation, but with greater magnitude than ENSO events. Especially warm and dry years happening due to an El Niño event could be the norm in the future (Lyra et al., 2017). Relating ecosystem carbon fluxes to El Niño and La Niña events, thus, can tell something about the carbon exchange in a future climate.

El Niño-Southern Oscillation is a natural, coupled atmospheric–oceanic cycle with a period length of about 2 to 7 years (Hanley et al., 2003). Normally, easterly trade winds blow warm surface water towards the western part of the Pacific Ocean, causing warm air to rise off the coast of Indonesia, which causes rainfall over the archipelago. During El Niño events, the easterly trade winds blowing towards Indonesia lessen or even change direction and the warm surface water flows towards the east resulting in increased sea surface temperatures (SST) in the central Pacific Ocean and decreased precipitation over Indonesia. During La Niña events, the opposite is the case, the strength of the easterly trade winds increases and warm surface water is driven farther to the west, increasing convection over the western Pacific Ocean and thereby rainfall over Indonesia (Cane and Zebiak, 1985). Different ways to define the manifestation and strength of an ENSO event have

been established. The most common indices to identify the different phases of ENSO are indices based on SSTs or the surface atmospheric pressure-based Southern Oscillation index (SOI) (Hanley et al., 2003; Trenberth, 1997). Through teleconnections, many parts of the world are affected by El Niño and La Niña events, changing their usual weather patterns and bringing droughts and floods. In Costa Rica, El Niño years result in decreased precipitation and increased temperatures during the summer months June to August (Fig. 1.1). La Niña years cause increased precipitation and decreased temperatures during the summer months June to August (Ropelewski and Halpert, 1987; Lyon and Barnston, 2005).
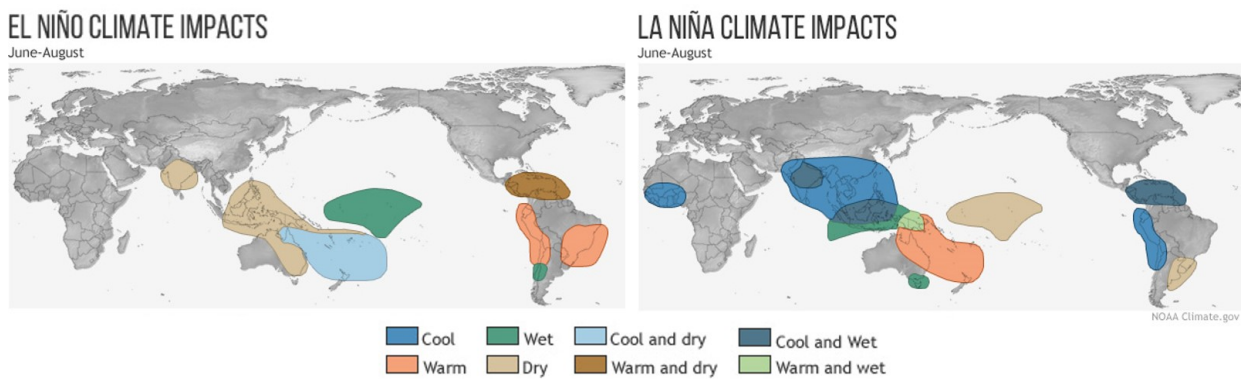
Figure 1.1.: Teleconnections of El Niño and La Niña events during the summer months June to August. Source: National Oceanic and Atmospheric Administration (NOAA), Climate.gov, `https://www.climate.gov/news-features/featured-images/global-impacts-el-nino-and-la-nina`

to date, research focus regarding the carbon balance has mostly been on tropical rain forests (Sánchez-Azofeifa et al., 2005), temperate and boreal forests. Some studies on tropical dry forests already exist, but mostly on sites with low annual precipitation, for example in Mexico (Verduzco et al., 2015; Perez-Ruiz et al., 2010) and Australia (Hinko-Najera et al., 2017). Although the interest in studies on tropical dry forest has grown since the beginning of the 21st century, due to the high complexity of the ecosystem, more research is still important to understand the carbon exchange dynamics in tropical dry forests (Portillo-Quintero et al., 2015).

The aim of this study was to analyze the carbon balance, i.e. the net ecosystem carbon exchange and the component fluxes, namely gross primary production and ecosystem respiration. The effects of the different states of the ENSO circulation and the different functional seasons were investigated. To help understand the connection between environmental drivers and the carbon balance, meteorological variables like precipitation and the turbulent energy fluxes, namely sensible heat flux and latent heat flux, and their relation to each other were examined. Friction velocity and roughness length were investigated to estimate the wind profile above the canopy and the strength of mixing. In order to connect the carbon fluxes directly to environmental forcings and to see which forcings are the main drivers for the carbon dynamics, the indices light use efficiency and water use efficiency were analyzed.

The research questions addressed in this thesis are therefore:

(1) What are the magnitudes of energy, and carbon fluxes and the net carbon balance? How do these fluxes vary if they are analyzed for the different functional seasons in tropical dry forests, i.e. wet and dry season? And what does the wind profile look like?
Regarding the carbon fluxes, it is hypothesized that the tropical dry forest at the study site is a net carbon source during dry seasons and a net carbon sink during wet seasons. For the wind profile, there are six different possible models, how the ecosystem could react to dry and wet season (Fig. 1.2).
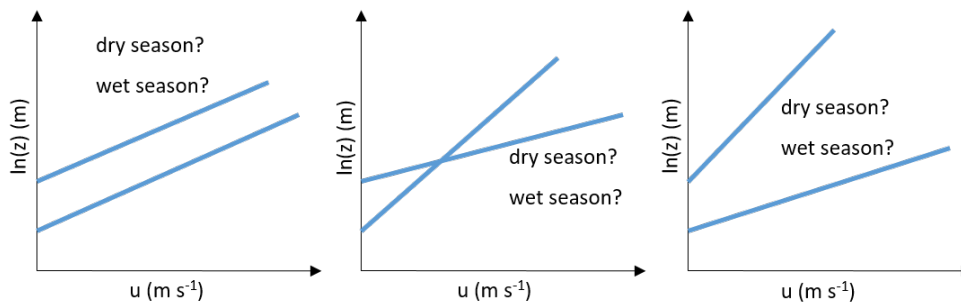
Figure 1.2.: Different concepts of how the logarithmic wind profile could vary for the functional seasons.
The blue lines show logarithmic wind profiles with different intercepts (natural logarithm of roughness length z_0) and slopes (inverse of friction velocity u_*).

(2) How and to which extent do ENSO events change the component carbon fluxes GPP and R_{eco} and their net carbon balance NEE?
The hypothesis is that in years with El Niño events, the NEE is less negative, i.e. the ecosystem is a smaller net carbon sink, due to the lower amount of precipitation. In La Niña years it is hypothesized that the NEE is more negative, i.e. the ecosystem is a greater net carbon sink, due to a higher water availability.

This work is a product of a collaboration between the research group of Prof. Dr. C. K. Thomas from the Micrometeorology group at the University of Bayreuth and the research group of Prof. Dr. G. A. Sànchez-Azofeifa and S. M. Castro from the Department of Earth and Atmospheric Science sat the University of Alberta, Canada.

2. Material and methods

2.1. Site description

2.1.1. Climate and vegetation

The study region is located within the biome Tropical and Subtropical Dry Broadleaf Forests as defined by Olson et al. (2001) after Holdridge's life zones. The temperatures range from 16 to 38 °C with higher temperatures during the dry season than during the rainy season, though due to prevailing higher wind speeds and dry winds, evaporative cooling reduces felt temperatures during the dry season (Janzen, 1986). Precipitation patterns in Costa Rica are mainly caused by the passage of the Intertropical Convergence Zone (ITCZ) (Sanford et al., 1994). Characteristic for the tropical dry forest in Santa Rosa National Park (SRNP) is a severe dry season from December to April/May when the ITCZ lays south of Central America, and a rainy season for the rest of the year when the equatorial low-pressure trough moves over Central America to the north, with total precipitation amounts of 915 to 2558 mm and a mean of 1614 mm from 1980 to 1989 (Janzen, 1986, 1993). In some years a shorter, less pronounced dry season occurs during the rainy season in summer, mostly in July and/or August, when the ITCZ is at its northern most position (Janzen, 1986). It is also called veranillo, "little summer", by the local people (see Sanford et al., 1994; Janzen, 1993; Daubenmire, 1972, for example).

The dry forest in the SRNP is deciduous forest of intermediate secondary succession about 30 years old (Sánchez-Azofeifa, pers. comm.), about 66 to 75 % completely or partly shed their leaves during the dry season (Frankie et al., 1974; Hubbell, 1979). The vegetation consisted of trees such as *Chochlospermum vitifolium*, *Vachellia cornigera*, *Bursera simaruba*, *Simarouba glauca*, *Crescentia cujete* and several *Cecropia* species, lianas and strangling figs (*Ficus aurea*) (Hubbell, 1979, and own field experience), the mean tree height was 10 m.

2.1.2. Study site

The study site is located in the SRNP in northwestern Costa Rica near the border to Nicaragua, about 40 km northwest of Liberia in Guanacaste Province (Fig. 2.1). The SRNP stretches from the Pacific Ocean at sea level to the Inter-American Highway at 350 m asl, which forms the eastern border, over coastal plains, plateaus, and canyons. The park, which was established in 1971, is part of a larger Conservation area, the "Area de Conservacion Guanacaste" (ACG) (Janzen,

1986). It consists of the National Parks Santa Rosa, Guanacaste and Rincón de la Vieja and spans ecosystems ranging from marine and coastal to dry tropical, tropical and tropical cloud forest.

The data for this study was collected at the Santa Rosa National Park-Environmental Monitoring Super Site (SRNP-EMSS) run by the collaborative research network Tropi-Dry. Two towers, Principe Tower at $10°51'15.3612''$ N, $85°36'29.16''$ W, $307\,\text{m}$ asl and Kaku Tower at $10°50'30.3612''$ N, $85°37'2.0388''$ W, $294\,\text{m}$ asl, are equipped with eddy covariance Systems.
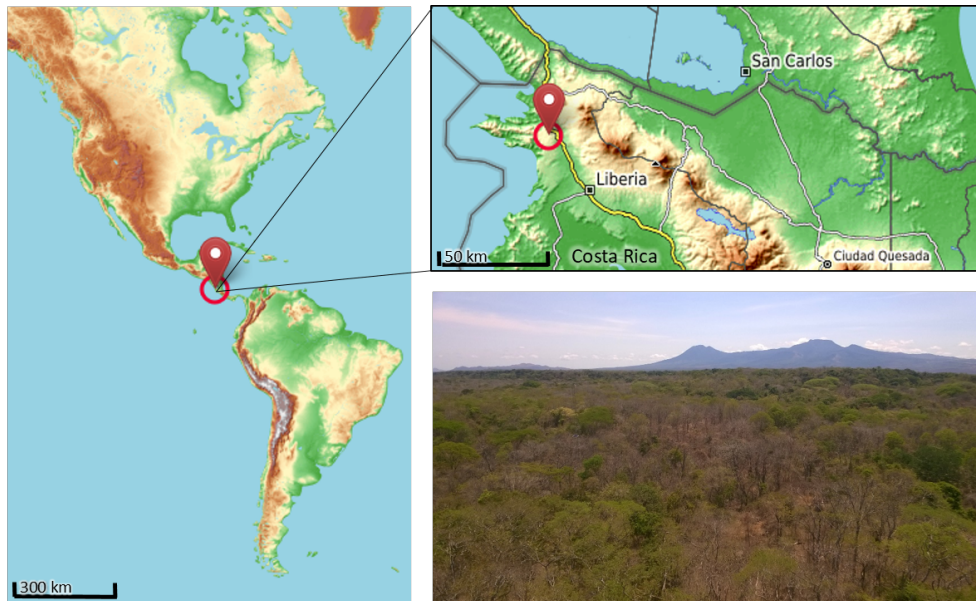
Figure 2.1.: Location of the study site and view over the tropical dry forest from Kaku tower at the end of the dry season. Adapted from OpenStreetMap, `https://www.opentopomap.org`.

2.2. Instrumentation and data acquisition

2.2.1. Eddy covariance data

Two eddy covariance (EC) Systems were used to gather three dimensional wind vector data, temperature, CO_2 concentration and water vapor concentration data at $10\,\text{Hz}$. The systems are mounted on the Kaku and Principe towers $30\,\text{m}$ agl. Both EC-Systems are closed-path eddy covariance flux systems (CPEC200, Campbell Scientific, Logan, UT, USA) consisting of a closed-path gas analyzer (EC155, Campbell Scientific, Logan, UT, USA), a 3-D sonic anemometer (CSAT3, Campbell Scientific, Logan, UT, USA) and a sample pump. A datalogger (CR3000, Campbell Scientific, Logan, UT, USA) on each tower recorded the data. Raw $10\,\text{Hz}$ data from Principe tower, referred to as "Principe tower BMM" in this work, as well as processed data with a resolution of $30\,\text{min}$ for Kaku tower, referred to as "Kaku tower", and for Principe tower, referred to as "Principe tower", were provided by the research group of Prof. Dr. G. A. Sànchez-Azofeifa and S. M. Castro

at the University of Alberta, Canada.

2.2.2. Weather data

Meteorological data with a resolution of 30 min, i.e., global radiation, reflected shortwave radiation, temperature, relative humidity, and precipitation, were also provided by the team of Prof. Dr. G. A. Sànchez-Azofeifa and S. M. Castro, measured at the SRNP-EMSS Meteo Tower. They are referred to as "Meteo tower" or "measured".

To compare the weather during the study period June 2013 to May 2017 to that over the last 30 years (1989 to 2018), weather model simulation data was provided by the commercial Swiss weather service provider meteoblue AG (`https://www.meteoblue.com`). Global historical weather data since 1985 with a resolution of 30 km is calculated with weather models based on the NOAA Environment Monitoring System (NEMS) technology, which allows the inclusion of detailed topography, ground cover and surface cover. Hourly data for global radiation, temperature, relative humidity, precipitation, wind speed, and direction were downloaded and used. They are referred to as "modeled".

2.2.3. Satellite data

The surface reflectances in the near-infrared waveband 1230 to 1250 nm and in the visible red waveband 620 to 670 nm were used to calculate the normalized difference vegetation index (NDVI). The data was monitored by the instrument MODIS (Moderate Resolution Imaging Spectroradiometer) which is installed on NASA's earth-observing satellite Terra. It was obtained from the NASA's Land Processes Distributed Active Archive Center (LP DAAC) and downloaded via the NASA EARTH SCIENCE DATA program AppEEARS (AppEEARS Team, 2019). Compositions of 8 days of surface spectral reflectance are available as Terra MODIS Bands 1 through 7 on AppEEARS. Bands 1 (620 to 670 nm) and 5 (1230 to 1250 nm) were downloaded and used to calculate NDVI (Vermote, 2015).

2.2.4. Sea surface temperatures

Anomalies in sea surface temperatures (SST) in the Niño 3.4 region in the Pacific ocean($5°$ N – $5°$ S, $120°$ W – $170°$ W) were used to identify El Niño and La Niña events. Running means of 3 months of SST anomalies were downloaded and used for the years 1989 to 2018 from the website of the National Weather Service Climate Prediction Center from the NOAA, `https://origin.cpc.ncep.noaa.gov/products/analysis_monitoring/ensostuff/ONI_v5.php`.

2.3. Data processing

2.3.1. Raw data processing

Turbulent fluxes and other variables such as 30 min averages of CO_2 concentration were computed from raw 10 Hz data from Principe tower BMM, using the MATLAB-application *bmmflux* (Thomas et al., 2009).

In the MATLAB-application *bmmflux*, spike detection and removal was done with the algorithm of Vickers and Mahrt (1997) by calculating moving averages and removing values that deviate more than 4.5 times the standard deviation.

To take account for sensor separation and sensor response the frequency response correction according to Moore (1986) was conducted and the wind coordinate system was rotated into the mean wind using the 3D-rotation after Wilczak et al. (2001).

Turbulent fluxes were calculated with the principles of Reynolds. According to Reynolds decomposition,

$$\overline{xy} = \overline{x}\,\overline{y} + \overline{x'y'} \tag{2.1}$$

with $\overline{x}$ and $\overline{y}$ as the means of the variables and x' and y' as the instantaneous deviations from the mean. The mean is calculated over a specific time interval, chosen as 30 min in this thesis. As the vertical wind speed is used as x for the calculation of fluxes and the coordinate system is rotated into the mean mean wind, such that $\overline{x} = 0$, Equation 2.1 can be simplified to:

$$\text{Flux} = \overline{x'y'} \tag{2.2}$$

with x as the vertical wind speed w (m s^{-1}) and y as CO_2 concentration c_{CO_2} (μmol m^{-2} s^{-1}) for the carbon dioxide flux FCO$_2$, sonic temperature T_s (K) for the buoyancy flux Q$_B$, specific humidity q (kg kg^{-1}) for the latent heat flux Q$_E$ and horizontal wind speed u (m s^{-1}) for the momentum flux τ. The friction velocity u_* was then calculated as generalized momentum flux and the sensible heat flux Q_H was calculated from Q_B using the Schotanus correction (Schotanus et al., 1983; Liu et al., 2001).

Additional to the calculation of fluxes, a quality assessment was applied checking if conditions that are necessary for the EC-method are met. Flux data was tested for stationarity as proposed by Foken and Wichura (1996) and developed turbulence as proposed by Thomas and Foken (2002) following the procedure of Foken et al. (2004). Quality assessment and quality control (QAQC) flags from 0 to 2 were assigned to the data. Flags of 0 indicate values that are suitable for basic scientific research, values with flag 1 can be used for long-term measurements of fluxes and values with flag 2 should only be used for orientation and should be excluded from further analysis. Data with QAQC flags of 2 were excluded from the analysis, as described in section 2.3.3.

Net ecosystem exchange (NEE) was then calculated from FCO_2 and CO_2 concentration as:

$$NEE = FCO_2 + F_{storage} \tag{2.3}$$

with the change in storage term estimated as:

$$F_{storage} = \int_{z_0}^{z_{30}} \frac{\partial c_{CO_2}}{\partial t} \tag{2.4}$$

with z_x as the measurement height in m agl.

2.3.2. Defining functional seasons

Seasonality influences phenology and carbon cycles and should therefore be accounted for when modeling and analyzing carbon and energy fluxes. In the tropical dry forest of SRNP, seasonality is caused by the alternation of wet and dry season. The phenology and carbon cycle of the vegetation strongly depend on onset, length and intensity of the rainy season. Using calendar seasons did not seem appropriate. Functional seasons and hydroecological years (HEY) were therefore defined according to the concept developed by Thomas et al. (2009) using the NDVI and Bowen ratio (Bo) (Fig. 2.2). NDVI (-) was calculated as:

$$NDVI = \frac{NIR - red}{NIR + red} \tag{2.5}$$

with 8-daily reflectance in the near-infrared range (NIR) (-) and 8-daily reflectance in the range of red visible light (-) (red). Daily Bowen ratios (-) were calculated from sensible heat flux (Q_H) and latent heat flux (Q_E) as:

$$\text{Daily } Bo = \frac{\text{Daily sum of } Q_H}{\text{Daily sum of } Q_E} \tag{2.6}$$

with daily sums of Q_H and daily sums of Q_E in $MJ\,m^{-2}\,d^{-1}$.

Four functional seasons were specified (Fig. 2.2). Rainy or wet seasons, transition periods and dry seasons were specified using the NDVI. The wet seasons lasted approximately from June to December. Transition periods were defined between wet seasons and dry seasons. The dry seasons lasted approximately from February to May. Veranillos, shorter, less pronounced dry seasons were specified using the Bowen ratio. They occurred during the wet season around July and were termed summer dry season in this work (see Tab. 2.1 and Fig. 2.2a). The end of the wet season was defined as the time of the maximum of NDVI before the steady decline of NDVI during the dry season. The end of the transition period was defined as the time when NDVI reached 0.8 during the steady decline of the NDVI during the dry season. The end of the dry season was defined as the time of the minimum of NDVI after the steady decline of NDVI during the dry season (Fig. 2.2b).
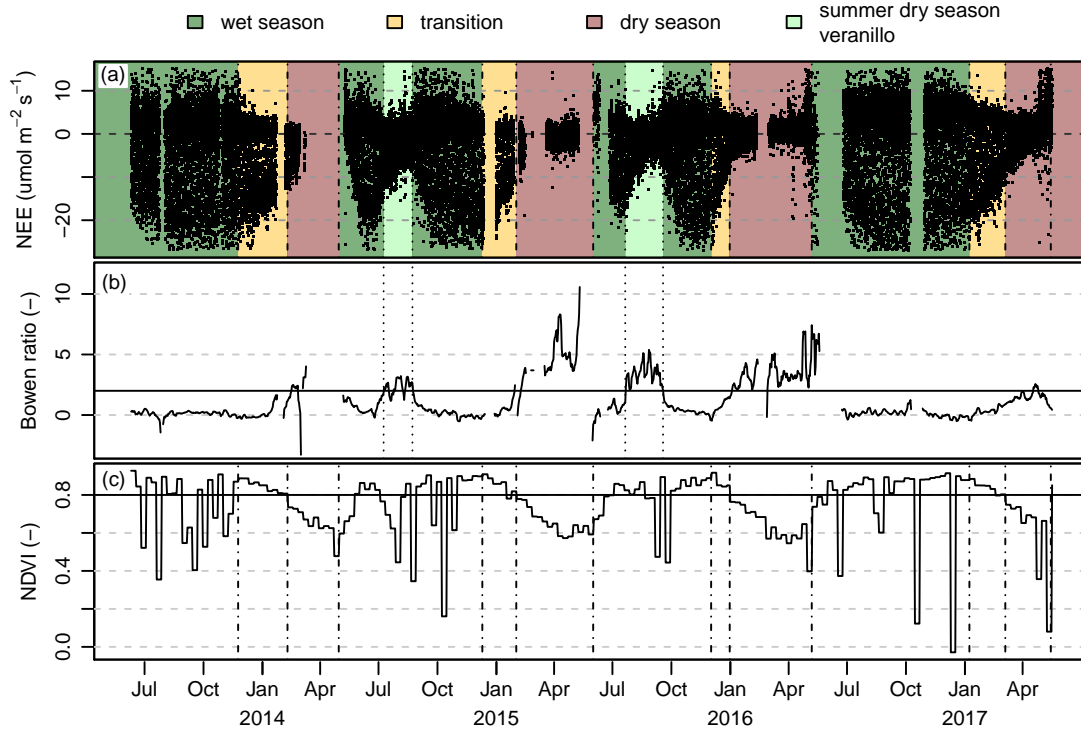
Figure 2.2.: Definition of Functional Seasons for Kaku tower. (a) functional seasons in NEE, classified according to (b) Bowen ratio and (c) NDVI.

Table 2.1.: Functional seasons and hydroecological years for the study period.

Season	2013			2014		
	Start	End	Length (days)	Start	End	Length (days)
wet season	Jun 8 2013	Nov 24 2013	168	May 1 2014	Dec 10 2014	178[a]
summer dry season	-	-	-	Jul 10 2014	Sep 23 2014	45
transition	Nov 25 2013	Feb 9 2014	77	Dec 11 2014	Feb 1 2015	53
dry season	Feb 10 2014	Apr 30 2014	80	Feb 2 2015	Jun 1 2015	120
total	Jun 8 2013	Apr 30 2014	325	May 1 2014	Jun 1 2015	396

Season	2015			2016		
	Start	End	Length (days)	Start	End	Length (days)
wet season	Jun 2 2015	Dec 2 2015	124[a]	May 8 2016	Jan 8 2017	245
summer dry season	Jul 22 2015	Sep 18 2015	59	-	-	-
transition	Dec 3 2015	Dec 31 2015	29	Jan 9 2017	Mar 5 2017	56
dry season	Jan 1 2016	May 7 2016	128	Mar 6 2017	May 15 2017	71
total	Jun 2 2015	May 7 2016	340	May 8 2016	May 15 2017	372

[a] Lengths of wet seasons are given excluding summer dry season.

Summer dry seasons were defined as the time when Bowen ratio exceeding 2 during the wet season. Two summer dry seasons were found, in 2014 and in 2015 (Fig. 2.2c). The start of a new hydroecological year was defined as the start of the wet season.

A simplified version of functional seasonality was used for the 30 years of modeled weather data. Only dry season and wet season were defined using precipitation. Dry season was defined as the time period with continuously less than 5 mm of precipitation per day. The start of the wet season together with the start of a new hydroecological year were defined as the first day with more than 5 mm precipitation.

2.3.3. Quality control

Prior to filling gaps to get complete time series of energy and carbon fluxes and further analysis and evaluation of the data, low-qualitiy-data and unphysical values were removed.

1. Values with QAQC flags of 2 as defined in section 2.3.1 were excluded.

2. For NEE, Q_E and Q_H hard thresholds were used to exclude exceedingly high or low values. Values lower than the 1st percentile and higher than the 99th percentile were set to NA (Tab. 2.2).

Table 2.2.: Hard thresholds for NEE, Q_E and Q_H, derived from the 1st and 99th percentile.

percentile	NEE ($\mu mol\,m^{-2}\,s^{-1}$)	Q_E ($W\,m^{-2}$)	Q_H ($W\,m^{-2}$)
1st	-27	-66	-91
99th	15	353	431

3. During calm night time periods, respiratory CO_2 fluxes captured with the eddy covariance method can be underestimated due to storage and advection (McHugh et al., 2017). To ensure sufficient mixing, u_* thresholds were applied to filter out data from calm night time periods following the approach by Reichstein et al. (2002). Thresholds of u_* were set in scatterplots of NEE against u_*, above which NEE became independent from u_* (Fig. 2.3). This was done separately for the functional seasons, summer dry season was considered as dry season (Tab. 2.3).

Table 2.3.: u_* thresholds.

functional season	u_* threshold ($m\,s^{-1}$)
wet season	0.2
transition	0.15
dry season	0.15

4. As the surrounding vegetation was quite homogeneous within the radius of a few km around the EC towers (Fig. 2.1), a footprint analysis was not conducted and data from all wind directions was used.
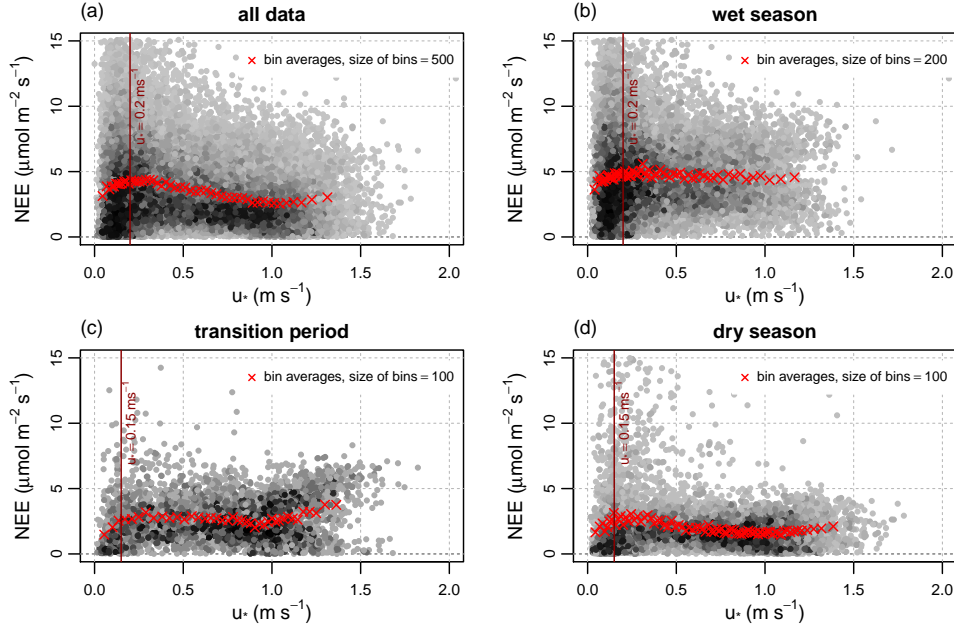
Figure 2.3.: NEE vs. u_* at Kaku tower for night time values (a) from the whole dataset and divided into the functional seasons (b) wet season, (c) transition period, and (d) dry season.
Summer dry season was considered as dry season. Only positive values smaller than 99th percentile were used. Light grey to black colors of the dots show the density, with black being highest density.

2.3.4. Gap filling and partitioning of carbon fluxes

To get complete weather data time series, gaps in global radiation and air temperature in the measured weather data set were filled using the modeled data. First, hourly modeled values were expanded to half hourly values using linear interpolation. Second, linear regression between modeled data and measured data was used to fill gaps in measured global radiation (Fig. 2.4a) and measured air temperature (Fig. 2.4c). Third, gaps in measured reflected radiation were filled by fitting a regression line between measured reflected radiation and measured global radiation and then modeling missing reflected radiation with the linear regression (Fig. 2.4b). This was done for wet season, transition period and dry season separately. Summer dry seasons were considered as transition period, because NDVI did not reach similarly low values in summer dry season as during the regular dry seasons, causing temperatures and reflected radiation to behave more similarly in the transition periods rather than in the dry seasons.

Gaps in NEE and ET time series that originated from instrument failure or data removal during quality control were then filled using the weather data. Gap filling and partitioning NEE into GPP
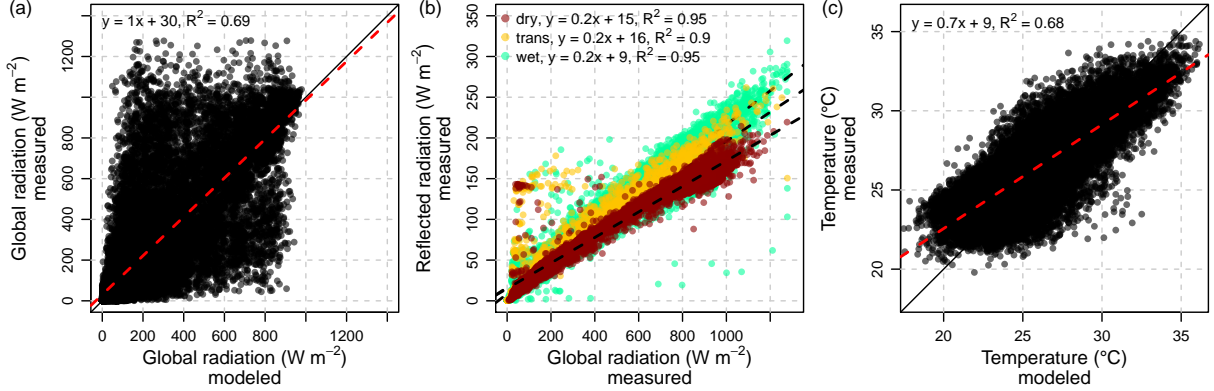
Figure 2.4.: Linear models between measured radiation and temperature data from Meteo tower and modeled data from meteoblue. (a) measured vs. modeled global radiation, (b) reflected shortwave radiation vs. global radiation, and (c) measured vs. modeled temperature.

and R_{eco} was done using the MATLAB-application *NEE-Tool-Terra*, also written by Prof. Dr. C. K. Thomas, with the following equations:

Gaps in daytime NEE were filled using a light response model after the Michaelis-Menthen-approach (Michaelis and Menten, 1913):

$$NEE = \frac{\alpha\,R_g\,F_{csat}}{\alpha\,R_g + F_{csat}} + R_{day}, \tag{2.7}$$

where α is photon use efficiency (-), R_g global radiation ($\mathrm{W\,m^{-2}}$), F_{csat} saturation NEE flux ($\mathrm{\mu mol\,m^{-2}\,s^{-1}}$) and R_{day} daytime bulk respiration ($\mathrm{\mu mol\,m^{-2}\,s^{-1}}$).

The model was fitted for each functional season separately and for different temperature classes. Summer dry season was combined with transition period because multiple runs showed better results than when combined with dry season. Details on the definition of temperature classes are given in appendix A.

During nighttime, NEE was assumed to consist only of respiration and was calculated with an arrhenius-type function after Lloyd and Taylor (1994):

$$NEE_{night} = R_{10}\,e^{E_0\left(\frac{1}{283.15 - T_0} - \frac{1}{T_a + 273.15 - T_0}\right)} \tag{2.8}$$

with R_{10} being the bulk respiration at a temperature of $10\,^{\circ}\mathrm{C}$ ($\mathrm{\mu mol\,m^{-2}\,s^{-1}}$), E_0 being the activation energy (K), T_0 being the reference temperature of $227.13\,\mathrm{K}$ and T_a being air temperature at $30\,\mathrm{m}$ agl ($^{\circ}\mathrm{C}$).

Gaps in latent heat flux (Q_E or evapotranspiration ET) were filled by using a linear regression fitting potential evapotranspiration (pET) calculated with Priestley Taylor against actual evapotranspiration (ET) (Priestley and Taylor, 1972; Thomas et al., 2009).
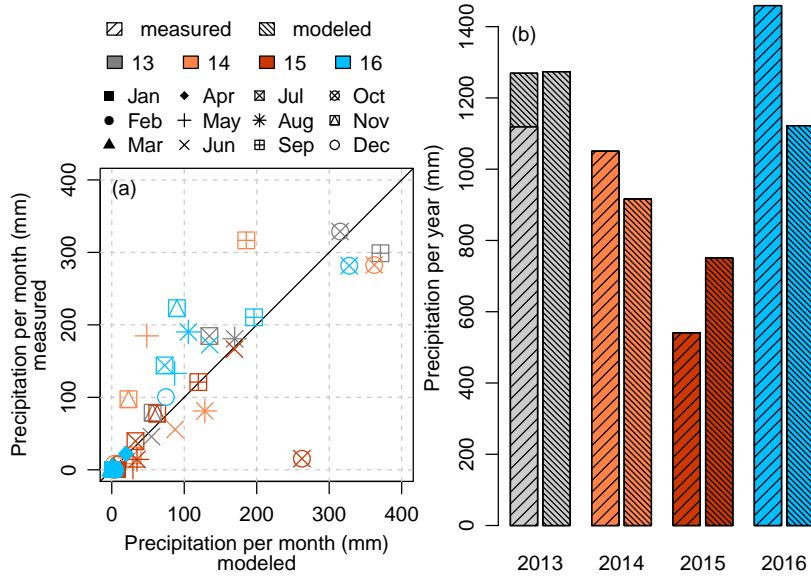
Figure 2.5.: Comparison between measured precipitation at Meteo tower and weather model simulations from meteoblue. (a) monthly sums as scatterplot and (b) annual sums as barplot.
In (b), missing data in measured precipitation at the beginning of the hydroecological year 2013 was replaced by modeled data, which is indicated by the hashed shaded bars.

$$ET = a \cdot ET_p + b = a \left(\alpha_{PT} \frac{R_{net} - Q_G}{\gamma \cdot s_c^{-1} + 1} \right) + b \tag{2.9}$$

with a (-) being the slope and b ($\mathrm{W\,m^{-2}}$) the intercept of the linear model. α_{PT} is the Priestley-Taylor coefficient (1.25 for wet season and 1.75 for dry season and transition period, (Shuttleworth, 2012)), R_{net} the net radiation in $\mathrm{W\,m^{-2}}$. Due to missing longwave radiation data, net radiation was estimated as $R_{net} \approx K_{net} = R_g - K \uparrow$ and longwave radiation was neglected. γ was calculated as:

$$\gamma \cdot s_c^{-1} = 1.042 \, e^{0.043 \, T_a} - 0.4. \tag{2.10}$$

2.3.5. Classification of ENSO phases

ENSO phases were classified according to the state of the El Niño Southern Oscillation for the years 1989 through 2018. The ENSO phases were defined with the Oceanic Niño Index (ONI) which is used by the NOAA. The ONI is based on anomalies in sea surface temperatures (SST) at the equator between South America and Indonesia. Running means of three months of SST anomalies in the Niño 3.4 region (5° N – 5° S, 120° W – 170° W) were therefore used. Warm (El Niño) and cold (La Niña) years were defined if the thresholds of +0.5 °C or −0.5 °C respectively

were exceeded for a minimum of 5 consecutive overlapping three-month periods, starting always with the three-month period May/June/July (MJJ). The 30 years were divided into 5 classes of neutral, weak, or strong El Niño and La Niña years respectively, if 3 of the 5 consecutive three-month periods exceeded the thresholds given in Table 2.4. The start of the year with MJJ was chosen for consistency with the definition of the hydroecological years, which start with the rainy season in about May.

Table 2.4.: Classification of ENSO events.

ENSO event	Abbreviation	Thresholds	# of years
Strong El Niño event	strong el niño	SST anomalies exceeded $+1.5\,^\circ$C	3
Weak El Niño event	weak el niño	SST anomalies of $+0.5$ to $+1.4\,^\circ$C	7
No ENSO event	no event	SST anomalies of less than $\pm0.5\,^\circ$C	9
Weak La Niña event	weak la niña	SST anomalies of -0.5 to $-1.4\,^\circ$C	7
Strong La Niña event	strong la niña	SST anomalies exceeded $-1.5\,^\circ$C	4
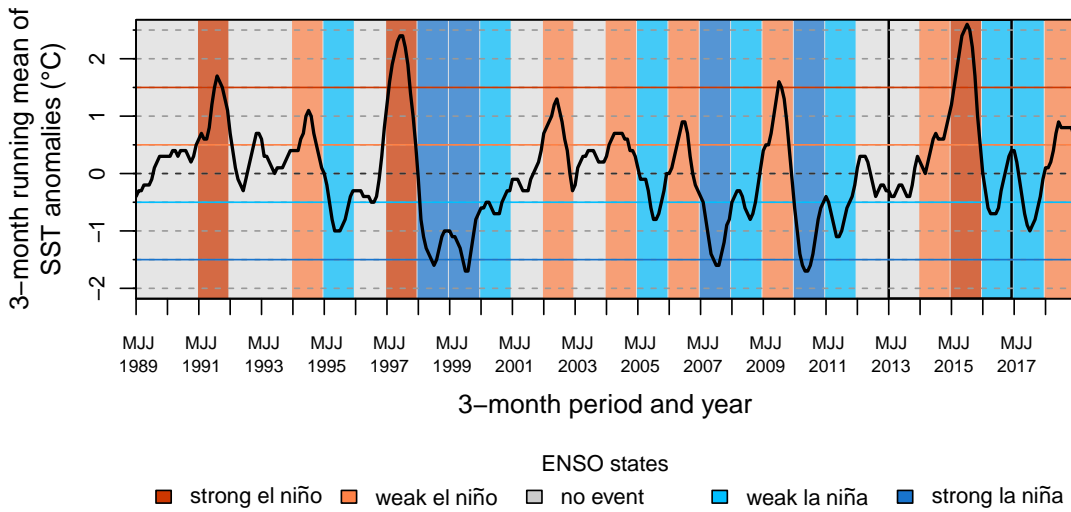
Figure 2.6.: Running mean of 3 months of SST anomalies. ENSO states in the 30 years from 1989 to 2018 are are shown as colored background and the thresholds as horizontal lines in the according colors. The study period from 2013 to 2016 is marked with vertical black lines.

The four years that were analyzed in this study fell in the classes "no event" (2013), "weak el niño" (2014), "strong el niño" (2015) and "weak la niña" (2016) (Fig. 2.6).

2.4. Conventions and calculations

As it is common in micrometeorology, the sign convention was used defining that positive fluxes (Q_E, Q_H and NEE) are always directed away from the surface and negative fluxes are directed to the surface. GPP and R_{eco} were always given a positive sign. Hence, $NEE = R_{eco} - GPP$.

Hydroecological years were defined as described in section 2.3.2. Whenever the terms "year" or "annual" are used in the following sections, they refer to hydroecological years, unless they are explicitly stated as calendar years.

Photosynthesis and transpiration are tightly coupled in green plants, as assimilation of carbon is always accompanied by transpiration of water and the amount of transpired water has to be matched by the water uptake through the roots. If soil water is depleted, plants (trees in forests more so than grassland) regulate the conductance of the stomata in order not to lose too much water. To quantify this trade-off, the ratio of the amount of carbon assimilated per amount of water transpired, called water use efficiency (WUE), is used (Eq. 2.11). On the ecosystem scale, assimilation and transpiration are replaced by the according ecosystem-scale quantities GPP and ET. Due to the non-linear response of vapor pressure deficit (VPD) on the stomatal conductance, inherent water use efficiency was analyzed additionally which takes into account the daily mean VPD during daylight time, 06:00 to 18:00 (Eq. 2.12). Following Beer et al. (2009), water use efficiency ($g_C \, kg_{H_2O}^{-1}$) was calculated as:

$$WUE = \frac{\text{Daily sums of } GPP}{\text{Daily sums of } ET} \tag{2.11}$$

and inherent water use efficiency ($g_C \, hPa \, kg_{H_2O}^{-1}$) was calculated as

$$IWUE = \frac{\text{Daily sums of } GPP \cdot \text{Mean daytime } VPD}{\text{Daily sums of } ET} \tag{2.12}$$

with daily sums of GPP in $g_C \, m^{-2} \, d^{-1}$, VPD in hPa and daily sums of ET in $kg_{H_2O} \, m^{-2} \, d^{-1}$.

Following the approach of water use efficiency, the ratio of net ecosystem exchange to evapotranspiration, called ecosystem water use efficiency (EWUE), was calculated as:

$$EWUE = \frac{\text{Daily sums of } NEE}{\text{Daily sums of } ET} \tag{2.13}$$

after Scott et al. (2006) and the ratio of ecosystem respiration to evapotranspiration, which was called respiration water use efficiency (RWUE) in this study, was calculated as

$$RWUE = \frac{\text{Daily sums of } R_{eco}}{\text{Daily sums of } ET} \tag{2.14}$$

with daily sums of R_{eco} in $g_C \, m^{-2} \, d^{-1}$ and daily sums of ET in $kg_{H_2O} \, m^{-2} \, d^{-1}$.

Additionally to the water supply, the available photosynthetic active radiation determines, how much carbon can be assimilated during photosynthesis. Light use efficiency (LUE) was calculated to quantify how much carbon is assimilated per photon of photosynthetic active radiation that reaches the plant. First, daily averages of GPP and PPFD (photosynthetic photon flux density) during daylight time, 06:00 to 18:00, were calculated. Then, LUE ($mol_C\,mol_{photon}^{-1}$) was calculated as:

$$LUE = \frac{\text{Mean daytime } GPP}{\text{Mean daytime } PPFD}. \tag{2.15}$$

with mean daytime GPP in $\mu mol_C\,m^{-2}\,s^{-1}$ and mean daytime PPFD in $\mu mol_{photon}\,m^{-2}\,s^{-1}$.

The roughness length was investigated to estimate the influence of foliage and no foliage on the wind profile. Roughness length is a length-scale representation of the roughness of a surface, related to the height of surface roughness elements. It is determined from extrapolating the logarithmic wind profile as the height, at which wind speed would theoretically become zero. To apply to cases with non-neutral stratification, the profile equations have to be extended by universal functions to take into account influences of buoyancy and shear. In the range of neutral conditions, profile equations are simplified as the universal functions get zero. Therefore, only near-neutral cases were used for the calculation of the roughness length.

To determine dynamic stability the stability parameter ζ was used, calculated from the Obukhov-Length L (after Obukhov, 1946; Monin and Obukhov, 1954). The Obukhov-Length L (m) and the stability parameter ζ (-) were calculated with the following equations.

$$L = -\frac{u_*^3}{\kappa \frac{g}{T_s} \overline{w'T_s'}} \tag{2.16}$$

$$\zeta = \frac{z}{L} \tag{2.17}$$

with the friction velocity u_* ($m\,s^{-1}$), κ, the von Kármán constant, as 0.4 (-) and g, the gravity acceleration, as $9.81\,m\,s^{-2}$. T_s is sonic temperature (K) , $\overline{w'T_s'}$ is the kinematic buoyancy flux ($K\,m\,s^{-1}$) and z is the height above ground (30 m agl). The dimensionless height ζ represents the dynamic stability derived from Monin-Obukhov theory. Only periods of near-neutral stability were then used to calculate the roughness length. Near-neutral stability was defined after Thomas et al. (2001) when $-0.2 < \zeta < 0.4$.

The roughness length z_0 was then calculated from the horizontal wind speed profile as:

$$u(z) = \frac{u_*}{\kappa} \ln\frac{z - d}{z_0} \quad \rightarrow \quad z_0 = \frac{z - d}{e^{\left(\frac{u(z) \cdot \kappa}{u_*}\right)}} \tag{2.18}$$

with $u(z)$ as wind speed in height z ($\mathrm{m\,s^{-1}}$), d the displacement height (m) and u_* the friction velocity ($\mathrm{m\,s^{-1}}$). The displacement height, which takes account of the displacement of zero wind speed due to the vegetation, was calculated as $\frac{2}{3}z_B = \frac{2}{3} \cdot 12\,\mathrm{m} = 8\,\mathrm{m}$. z_B is determined using the tallest $10\,\%$ of the trees, which was estimated as $12\,\mathrm{m}$. This means that the magnitude of the calculated roughness length is not completely accurate. The course of z_0 though is not altered by this uncertainty and was used for analysis.

To estimate, how much of the turbulent mixing is contributed by buoyancy from differences in water vapor concentration in contrast to temperature differences, the virtual temperature and the proportion that is made up of water vapor concentration. were calculated with the following equations. Virtual temperature T_v (K) was calculated as:

$$T_v = T_{sonic} \cdot \left(1 + 0.38 \cdot \frac{e}{p} \right) \tag{2.19}$$

and the proportion of vapor pressure contribution in T_v was calculated as:

$$\frac{\left(T_{sonic} \cdot 0.38 \cdot \dfrac{e}{p} \right) \cdot 100\,\%}{T_v} \tag{2.20}$$

with T_s being sonic temperature K), e being vapor pressure (hPa) and p being atmospheric pressure (hPa).

All calculations were done using the free statistics software R (R Core Team, 2018) with the packages "zoo" (Zeileis and Grothendieck, 2005), "vioplot" (Adler and Kelly, 2018) and "plotrix" (Lemon, 2006).

2.5. Uncertainty in EC measurements

The total flux measurement error is a composite of systematic errors, or bias, and random errors.

Systematic errors can arise from instrumentation and sampling, like instrument separation or incomplete spectral response, from terrain and vegetation, like underestimation of nocturnal fluxes or footprint heterogeneity or from other factors. These systematic errors are addressed by applying a frequency response correction or by filtering night time data by a u_* criterion. Known systematic errors were treated as described in sections 2.3.1 and 2.3.3.

To quantify the random error, an uncertainty analysis was conducted following the two tower approach by Hollinger and Richardson (2005). The measurement uncertainty, or random error, δ, was calculated as the differences between simultaneously measured fluxes from the two towers Principe and Kaku, which are $1.9\,\mathrm{km}$ apart. Histograms were plotted to determine the probability distribution (Fig. 2.7). Furthermore, median, standard deviation, skewness and kurtosis were calculated (Tab. 2.5). As the distribution of the measurement uncertainties fit a Laplace distribution

better than a Gaussian distribution, the standard deviation for a Laplace distribution, $\sqrt{2}\,\beta$, was calculated as the equivalent to the standard deviation σ for a Gauss distribution (Richardson et al., 2006). The scale parameter β was calculated as:

$$\beta = \frac{1}{N}\sum_{i=1}^{N}|x_i - \overline{x}|. \tag{2.21}$$

Table 2.5.: Properties of measurement uncertainties (δ) for FCO_2, Q_H and Q_E calculated from simultaneous measurements from Principe tower and Kaku tower.

	median	$\sqrt{2}\,\beta^a$	skewness	kurtosis[b]	n
$\delta\ FCO_2$	0.4	5	0.6	4.8	2822
$\delta\ Q_H$	0.6	57.9	1.8	5.2	2859
$\delta\ Q_E$	-1.4	61	-0.3	7.8	2843

[a] As the probability density function of the measurement uncertainties fit a Laplace distribution better than a Gaussian distribution, $\sqrt{2}\,\beta$, was used as the equivalent to σ for a Laplace distribution.

[b] Kurtosis is excess kurtosis (kurtosis - 3, for better comparison with normal/Gaussian distribution which has a kurtosis of 3.)
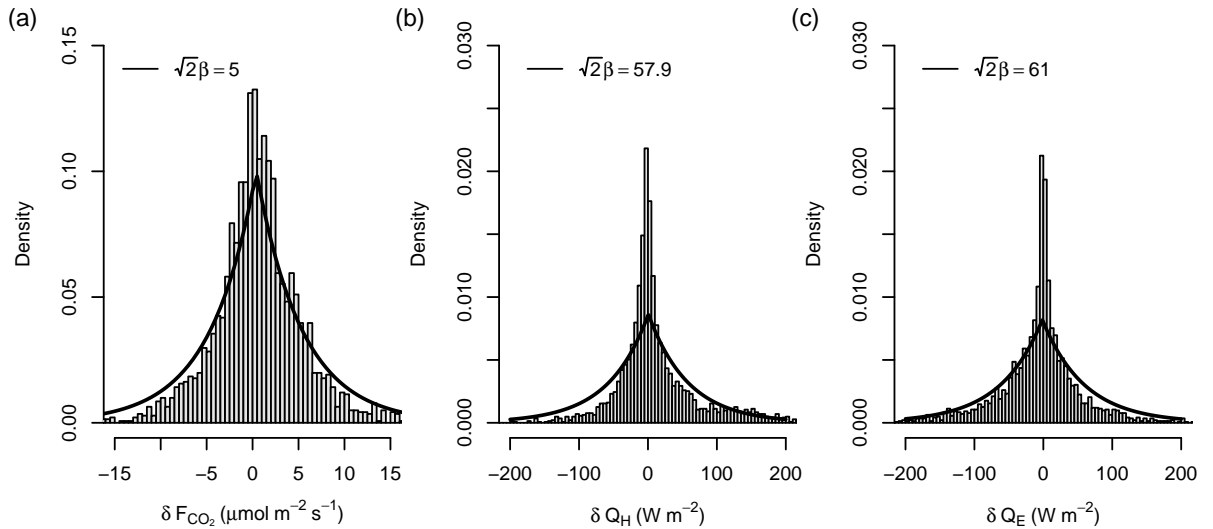
Figure 2.7.: Distribution of measurement uncertainties (δ) for (a) F_{CO_2}, (b) Q_H, and (c) Q_E. Probability density functions better fitted double exponential (Laplace) distribution than normal/Gaussian distribution, with strongly leptokurtic sides, a pronounced peak and long tails. Solid lines show Laplace distributions with the equivalent to σ, $\sqrt{2}\,\beta$, for a Laplace distribution.

The median of δ was close to zero for FCO_2 and Q_H and slightly higher for Q_E with $-1.4\,\mathrm{W\,m^{-2}}$ (Tab. 2.5). $\sqrt{2}\,\beta$ for FCO_2 was $5\,\mathrm{\mu mol\,m^{-2}\,s^{-1}}$. This equals about $19\,\%$ of the maximum net CO_2 uptake of $-27\,\mathrm{\mu mol\,m^{-2}\,s^{-1}}$ (see 1st percentile of NEE in Tab. 2.2). For Q_E and Q_H, $\sqrt{2}\,\beta$ was

about $60\,\mathrm{W\,m^{-2}}$. This equals approximately 17 and $14\,\%$ of the maximum latent and sensible heat fluxes of 353 and $431\,\mathrm{W\,m^{-2}}$, respectively (see 99th percentiles of Q_E and Q_H in Tab2.2). The distribution of δ for FCO_2 showed a skewness of 0.6 and is therefore moderately skewed right. The distribution of Q_E was with a skewness of -0.3 quite symmetrical. The skewness for Q_H was 1.8, indicating a highly right skewed distribution. Excess kurtosis ranged between 4.8 and 7.8, indicating leptokurtic distributions (Tab. 2.5) (Bulmer, 1979).

Furthermore, two linear regressions were conducted. First, for fluxes from the two towers Principe and Kaku, both calculated by Castro et al. (2018). And second, for fluxes from Principe tower calculated by Castro et al. (2018) and fluxes from Principe tower BMM, calculated with the MATLAB tool *bmmflux*.
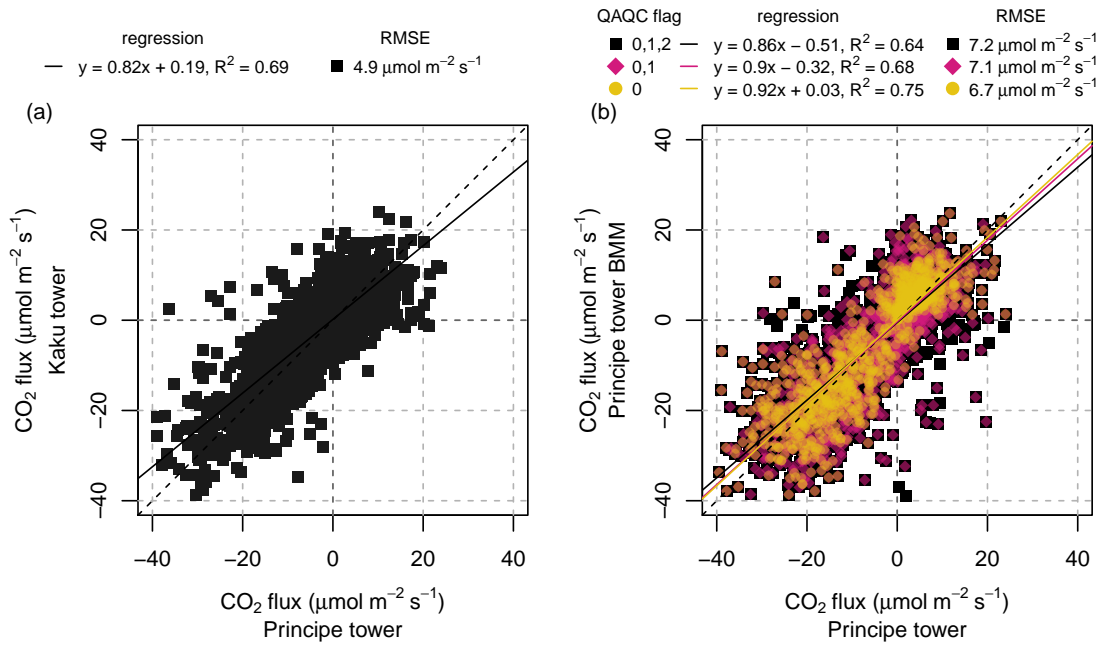
Figure 2.8.: Comparison of (a) CO_2 fluxes from Kaku tower and Principe tower, processed by Castro et al. (2018) and (b) CO_2 fluxes from Principe tower BMM, processed with *bmmflux* and Principe tower, processed by Castro et al. (2018).
The dashed line represents the 1:1 line, the solid lines show the regression lines. In (b), black indicates QAQC flags 0, 1 and 2, pink indicates QAQC flags 0 and 1, and yellow indicates QAQC flag 0 only.

The comparison of the CO_2 fluxes from the two EC towers Principe and Kaku showed a good correlation of $R^2 = 0.83$ and a small root mean square error (RMSE) of $4.9\,\mathrm{\mu mol\,m^{-2}\,s^{-1}}$ (Fig. 2.8a). The slope of the regression line was 0.82 with an intercept of $0.19\,\mathrm{\mu mol\,m^{-2}\,s^{-1}}$.

The comparison between different processing methods for raw data from the same tower, Principe tower, yielded larger root mean square errors of 6.7 to $7.2\,\mathrm{\mu mol\,m^{-2}\,s^{-1}}$ (Fig. 2.8b). Linear regression yielded slopes of 0.86, 0.9 and 0.92 with intercepts ranging from -0.51 to $0.03\,\mathrm{\mu mol\,m^{-2}\,s^{-1}}$

for all data (quality flags 0, 1 and 2), data with higher quality (quality flags 0 and 1), and only highest quality (quality flag 0 only), respectively. The CO_2 fluxes that were calculated with the *bmmflux* application were slightly smaller than the CO_2 fluxes calculated by Castro et al. (2018). Using only data with higher quality resulted in smaller RMSE and improved the correlation.

In summary, fluxes calculated with the same processing tool but from two towers about 2 km apart show small root mean square errors but larger deviation from the 1:1 line, and fluxes calculated with different processing tools but from the same tower show better agreement with the 1:1 line but higher root mean square errors.

3. Results

3.1. Climatic conditions

3.1.1. Hydroecological years and functional seasons
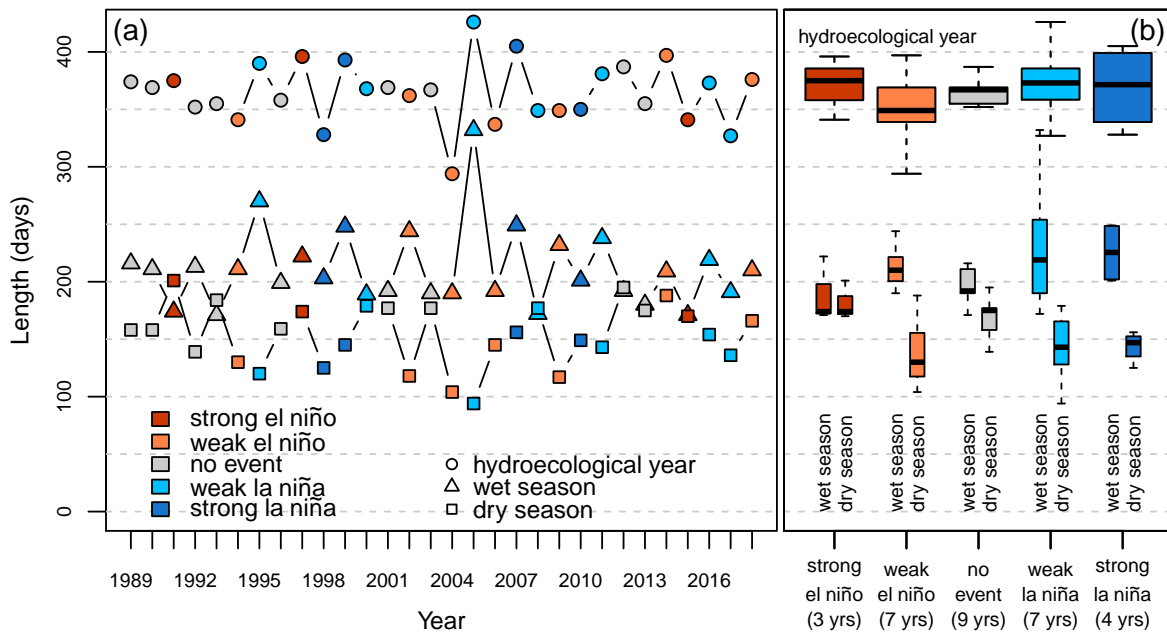
Figure 3.1.: Statistics for duration of hydroecological year, wet season, and dry season, divided into ENSO classes as (a) time series and (b) boxplot.

Hydroecological years and functional seasons were defined for the 30 years from 1989 to 2018 according to the procedure described in section 2.3.2. Durations of hydroecological years varied from 294 to 426 d but did not show significant differences between El Niño or La Niña years (Fig. 3.1). The length of the wet season ranged between 171 and 332 d. Dry seasons varied between 94 and 201 d in duration. During years with strong El Niño and with no ENSO event, wet season and dry season were in median similarly long. In contrast, the wet season was in median significantly longer than the dry season during years with weak El Niño, weak La Niña and strong

La Niña (Fig. 3.1b). The hydroecological year 2005 was exceptionally long with 426 d and also had an exceptionally long wet season with 332 d. The dry season was correspondingly the shortest with 94 d (Fig. 3.1a).

3.1.2. Precipitation
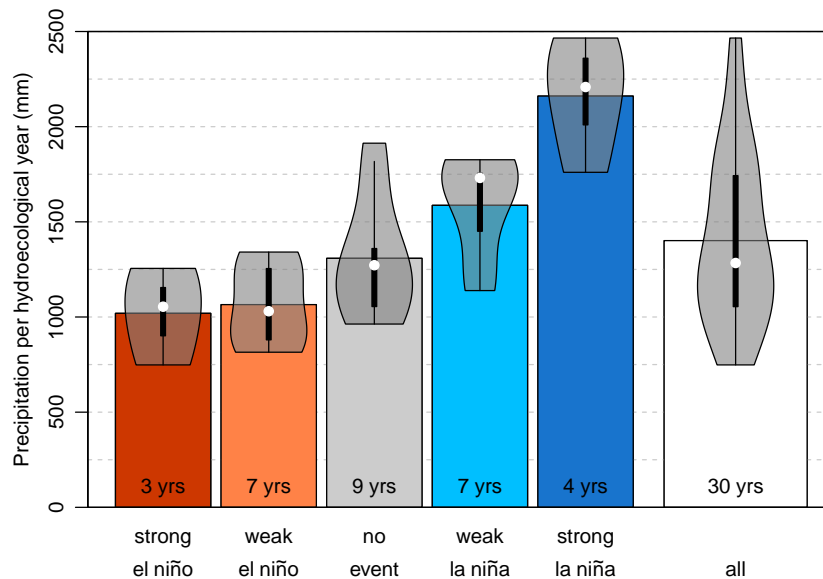
Figure 3.2.: Statistics for modeled precipitation from 1989 to 2018. The bars show the mean of annual precipitation across all 30 years and divided into ENSO states. Violin plots show the distribution, the median as white dot and the interquartile range as thick black line. Annual sums were calculated over hydroecological years as defined in section 2.3.2.

Modeled precipitation from weather model simulation mostly can not reproduce small-scale patterns in space and time. But annual sums over a longer period of time can still be used to find broader patterns. A clear pattern depending on ENSO events could be seen in the distribution of annual sums of modeled precipitation over the last 30 years (Fig. 3.4). Annual sums of modeled precipitation were calculated over hydroecological years, which start with the onset of rainfall and end with the end of dry season, as defined in section 2.3.2. The average of annual precipitation sums for years with no ENSO event was about as high as the average of annual precipitation sums across the complete reference period of 30 years, which was 1400 mm. Lowest annual sums of precipitation were found during strong and weak El Niño years, about 30 % less than the mean across all 30 years. Highest annual sums were found during strong La Niña years, 54 % more than the mean across all 30 years. But also in years with weak La Niña, precipitation sums were still 13 % higher than the mean across all 30 years. The distribution of annual rainfall sums across all 30 years showed two maxima corresponding to the distinct differences in rainfall sums for El Niño and La Niña years.

3.1.3. Wind speed and direction
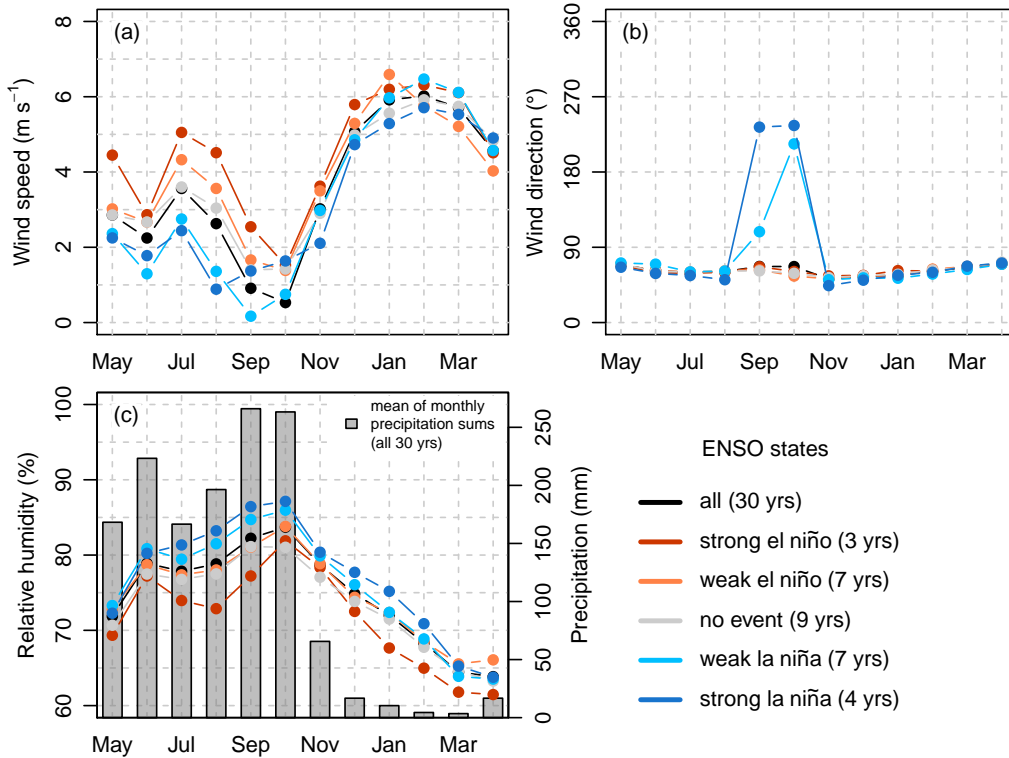
Figure 3.3.: Climate statistics for 1989 to 2018 for (a) wind speed, (b) wind direction, and (c) relative humidity. Displayed are monthly means. Bars in (c) indicate mean monthly precipitation sums over all 30 years.

Maximum mean wind speeds of $6\,\mathrm{m\,s^{-1}}$ were observed for the dry season in the months of Jan/Feb/Mar (Fig. 3.3a). Lower wind speeds of 1 to $3\,\mathrm{m\,s^{-1}}$ were found for the wet season in the months of May/Jun and Sep/Oct/Nov. A second maximum with monthly mean wind speeds of $4\,\mathrm{m\,s^{-1}}$ could be seen in July and August. Generally, La Niña years showed lower wind speeds than the mean across all 30 years and El Niño years showed slightly higher wind speeds. This phenomenon was especially pronounced during the time of summer dry seasons in the months of Jul/Aug, where monthly mean wind speeds ranged between $1\,\mathrm{m\,s^{-1}}$ in strong La Niña years and $5\,\mathrm{m\,s^{-1}}$ in strong El Niño years.

Mean wind directions were found to be very consistent throughout the year (Fig. 3.3b). They changed only slightly from almost easterly winds in May to north easterly winds in November and then back to easterly winds. This pattern could be observed for the monthly means across all 30 years, years with no ENSO event, for years with weak and with strong El Niño events. In years with weak La Niña events a deviation was observed, when wind directions changed to south easterly winds in September and almost south westerly winds in October. In strong La Niña years,

the deviation was even stronger. Mean wind directions were in September and October south west.

3.1.4. Relative humidity

Minimum monthly means of relative humidity across all 30 years were observed at the end of the dry season in the months of Mar/Apr with 63 % (Fig. 3.3c). With the beginning of the wet season in May, relative humidity increased rapidly to 80 % in June. Maximum monthly mean relative humidity of 87 % was found at the end of the wet season in October, when mean monthly precipitation was also highest. Then, relative humidity decreased steadily during the dry season until March. The influence of the ENSO circulation was visible in relative humidity, too. Higher monthly means of relative humidity were found in years with strong La Niña events and lower monthly means in years with strong El Niño events. The difference was especially pronounced for the months of Jul/Aug, the time of year when summer dry seasons occur.

3.1.5. Temperature

Daily means of modeled temperature ranged between 19.4 and 29.7 °C (Fig. 3.4). Maximum mean daily temperatures were observed at the beginning of the wet season in May. During the wet season, mean daily temperatures decreased constantly. Minimum mean daily temperatures were found at the end of the wet season in Dec/Jan. A clear pattern depending on ENSO events could also be detected in monthly medians of mean daily temperatures. Higher monthly median temperatures were found in El Niño years and lower monthly median temperatures in La Niña years. The effect of summer dry seasons was also noticeable as slightly increased temperatures in August, especially during strong El Niño years.
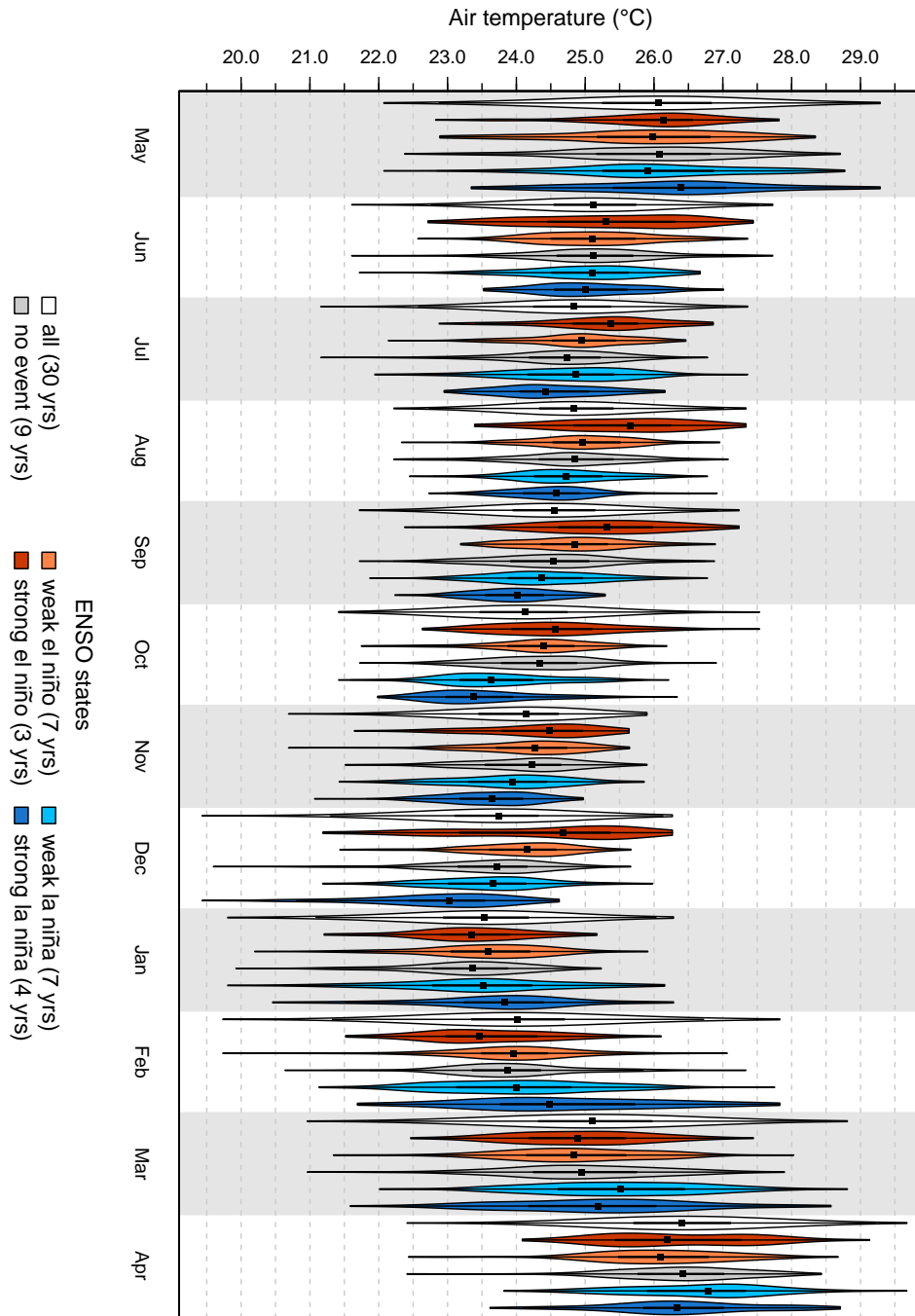
Figure 3.4.: Statistics for air temperature from 1989 to 2018. Violin plots show the distribution of daily mean air temperatures per month across all 30 years and divided into the ENSO classes.

3.2. Turbulent energy fluxes and precipitation

3.2.1. Amount and distribution of precipitation during the study period
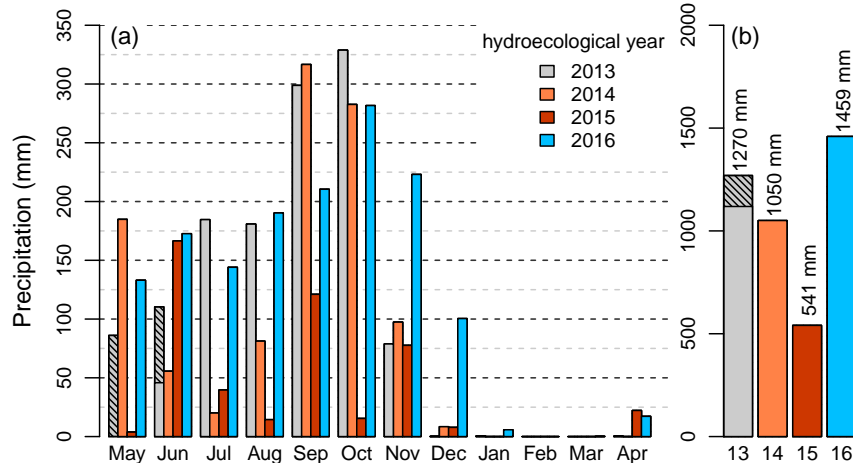
Figure 3.5.: Cumulative precipitation as (a) monthly sums and (b) annual sums for the study period. Bar sections with shading lines in (a) and (b) indicate missing values in the precipitation time series for Meteo tower, they were replaced with modeled precipitation.

Measured precipitation in a specific, small area and over a short time period can differ greatly from modeled precipitation from weather model simulation data (see Fig. 2.5). To compare precipitation sums during the study period and relate them to ENSO circulation effects, measured precipitation from the study site was investigated. Annual sums of measured precipitation varied strongly in SRNP during the study period. Annual sums ranged between 541 mm in 2015 and 1459 mm in 2016 (Fig. 3.5b). The year 2015 with the strong El niño event had about 60 % less precipitation than the mean across all 30 years (modeled precipitation, see sec. 3.1.2). Monthly precipitation sums showed a rainy period from May to November and a dry period from December to April (Fig. 3.5a). In the years of 2013 and 2016, monthly precipitation sums increased during the rainy period and maximum sums were found in October. In 2014 and 2015, monthly precipitation sums were distinctly reduced in the months of Jul/Aug, indicating a summer dry season.

3.2.2. Evapotranspiration

A great part of the precipitation goes into transpiration from plants and evaporation from leaf and soil surfaces, i.e. the evapotranspiration. ET sums for the whole hydroecological years of 2013, 2014 and 2015 were very similar with 547 mm, 570 mm and 476 mm, respectively (Fig. 3.6). Here, annual evapotranspiration sums mostly depended on the length of the season. In the years 2014 and 2015, a small offset arose during the summer dry seasons compared to 2013, due to a slightly decreased slope of cumulative ET in summer dry seasons. In the year 2014, this offset
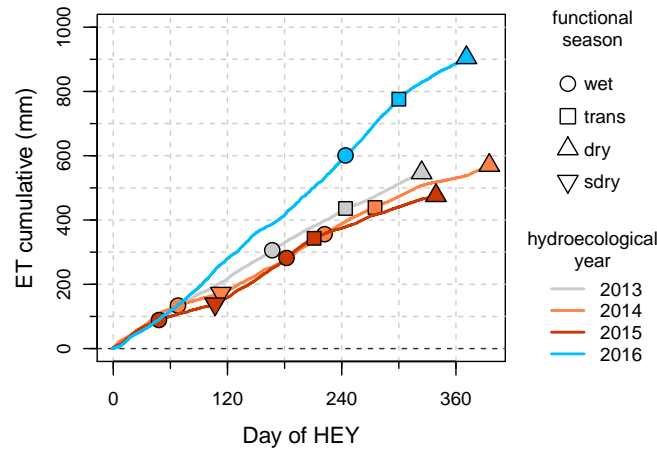
Figure 3.6.: Cumulative ET over the functional seasons, divided into the four hydroecological years. The symbols display the end of the functional season.

was compensated and even slightly exceeded due to the elongated hydroecological year. Maximum cumulative ET of 905 mm was found in 2016, which is almost twice as much as in the other three years. Here, the slope of cumulative ET was significantly steeper and even increased during the transition period.

3.2.3. Surface water balance
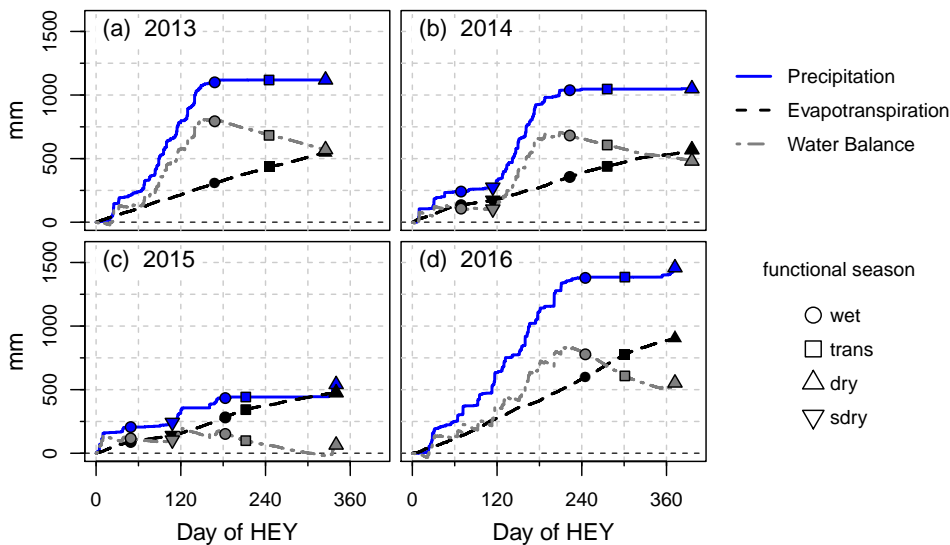
Figure 3.7.: Cumulative precipitation, evapotranspiration, and surface water balance for the four hydroecological years (a) 2013, (b) 2014, (c) 2015, and (d) 2016.

The surface water balance was calculated as precipitation minus evapotranspiration. It can be used as an estimate for soil moisture, but as runoff is not taken into account, it is only an

approximation. The surface water balance can help to estimate how much soil moisture is still available for the plants during the course of the dry season, which sustains GPP beyond the wet season. A net water gain ranging from 481 to 571 mm was found for the years 2013, 2014 and 2016. In the year of 2015, precipitation was much lower, but evapotranspiration was found to be about as high as in the other three years. This resulted in a net water gain of only 65 mm.

3.2.4. Latent heat flux, sensible heat flux and Bowen ratio
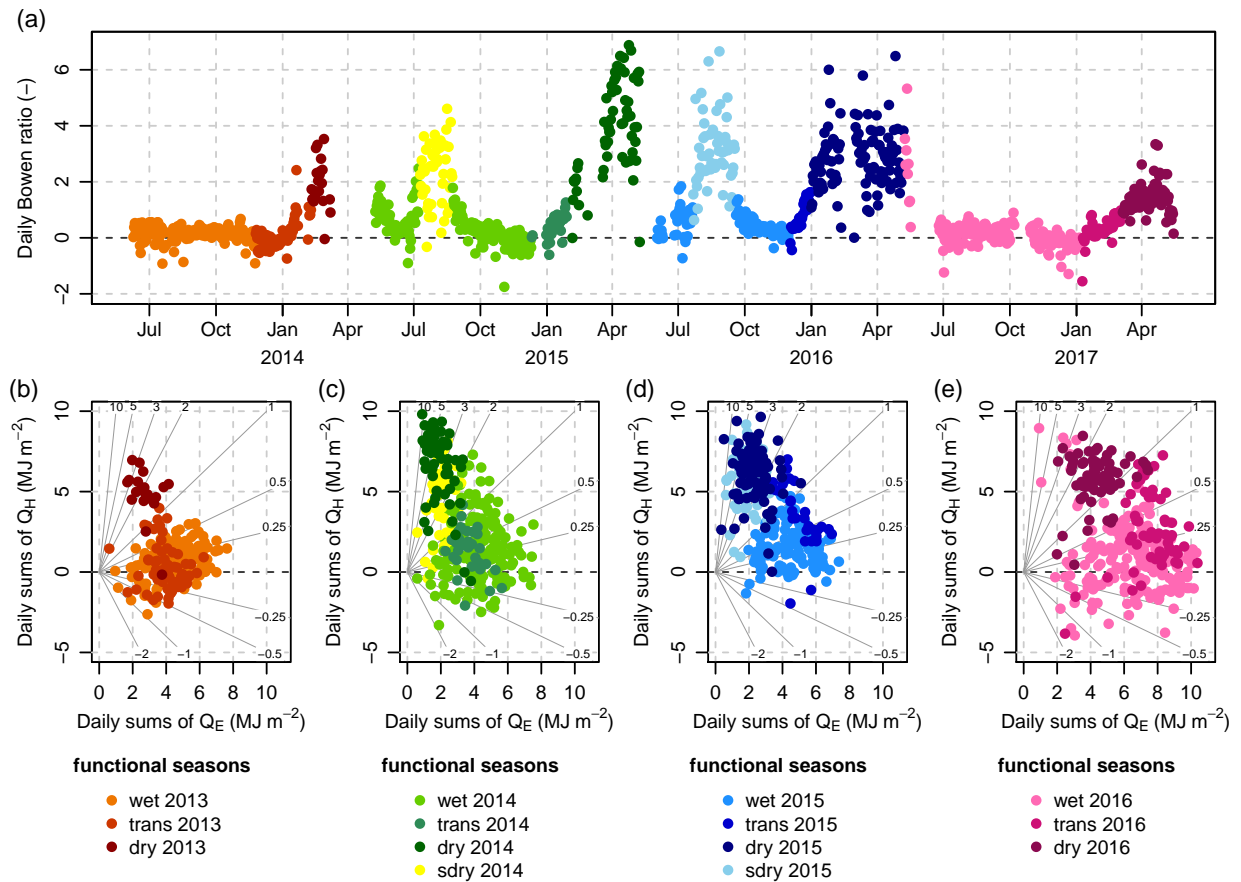
Figure 3.8.: Daily Bowen ratios at Kaku tower as (a) time series for the study period and scatterplots of mean daytime Q_H against mean daytime Q_E for the four hydroecological years (b) 2013, (c) 2014, (d) 2015, and (e) 2016.
Slanted lines in (b), (c), (d), and (e) depict Bowen ratio.

Evapotranspiration is not only part of the surface water balance but evapotranspiration or latent heat flux and sensible heat flux are also important components of the surface energy balance. They show how much energy reaching the surface in the form of incoming shortwave radiation is converted to turbulent fluxes of heat and water vapor. The Bowen ratios show the relationship between both. Daily Bowen ratios were calculated using equation 2.6 and ranged between −2 and

Table 3.1.: Daily Bowen ratios at Kaku tower per functional season.

Functional season	2013	2014	2015	2016
wet season	0.14	0.37	0.43	0.18
summer dry season	-	2.36	2.92	-
transition	0.10	0.41	0.77	0.32
dry season	1.92	3.49	2.76	1.40

10 (Fig. 3.8a). Negative Bowen ratios mainly occurred during wet season and transition period, when negative sensible heat fluxes of up to $-4\,\mathrm{MJ\,m^{-2}\,d^{-1}}$ were reached. Maximum daily Bowen ratios of up to 10 were observed during the dry season due to high daily sums of sensible heat flux and low daily sums of latent heat flux. Mean Bowen ratios were always significantly higher in the dry season than in the wet season of the same year (Mann-Whitney U test, $p < .001$ for all four years). The Mann-Whitney U test was used to determine the significance of differences as frequency analyses indicated that the daily Bowen ratios are not normally distributed (Shapiro-Wilk test, $p < .001$). In the drier years 2014 and especially 2015, Bowen ratios during wet season, transition period and dry season were significantly higher than in those seasons of the year 2013 (Mann-Whitney U test, $p < .001$ for all three seasons) (Tab. 3.1).

3.2.5. Turbulent forcing through evapotranspiration

I also wanted to investigate how much the differences in water vapor concentration contribute to the turbulent mixing compared to the buoyancy from temperature differences. As air with higher absolute humidity is less dense than air with lower absolute humidity, and during the rainy season absolute humidity is higher, this effect could add to the turbulent mixing. Virtual temperature was therefore calculated with equation 2.19. Then, the percentage of virtual temperature that was contributed by water vapor concentration was calculated with equation 2.20. The contribution was found to be very small (Fig. 3.9).

The proportion of T_v that was contributed by water vapor ranged between 0.85 % and 1.06 %. Transition periods and dry seasons showed with 0.85 to 0.92 % the lowest percentage of water vapor contribution. The transition period in 2015 and the dry season in 2016 were found to be exceptions and showed percentages of 0.97 and 1.01 % water vapor contribution. Mean virtual temperatures for the different functional seasons ranged between 29.9 °C (303.1 K) and 32.1 °C (305.2 K) (Fig. 3.9). They were highest for dry seasons and summer dry seasons and lower for wet seasons and transition periods. The transition period in 2015 was an exception here, too, as it showed a mean virtual temperature of 32.1 °C.

Figure 3.9.: Virtual temperature T_v against the proportion that is contributed by water vapor.

3.2.6. Wind profile characteristics

Friction velocity is a generalized momentum flux and thus describes the transport of turbulent kinetic energy. Hence, it can be counted as an energy flux. The roughness length was calculated with Equation 2.18 to investigate, how the foliage influences the turbulent mixing above and within the canopy. Median roughness lengths over the functional seasons varied from 0.6 m to 1.1 m with smallest z_0 for wet seasons and greatest z_0 for dry seasons (Fig. 3.10b). Over the study period, the roughness length was smallest at the beginning of transition periods with 0.3 m and then increased over the transition periods to reach highest values in the middle of the dry seasons with 1.7 m for May 2015 (Fig. 3.10a). During the summer dry seasons the roughness length showed a local maximum. During the dry season of 2016, the roughness length did not show as high values as in the dry seasons of the years 2013, 2014 and 2015.

Plotting friction velocity against mean wind speed showed hockey-stick-shaped curves with friction velocity depending linearly on mean wind speed in the strong-wind regime and no dependency in the weak-wind regime (Fig. 3.11). A weak-wind regime could be detected from the section of independent u_* below about $2\,\mathrm{m\,s^{-1}}$. The threshold varied slightly for the different functional seasons from 1.87 to $2.39\,\mathrm{m\,s^{-1}}$. Also, mean wind speed and friction velocity were generally higher during transition period and dry season than during wet season (see the black dots at about $6\,\mathrm{m\,s^{-1}}$ mean wind speed and $1\,\mathrm{m\,s^{-1}}$ friction velocity in Figures 3.11c and d).

functional season

◻ wet 2013	◻ wet 2014	◻ wet 2015	◻ wet 2016
◻ trans 2013	◻ trans 2014	◻ trans 2015	◻ trans 2016
◻ dry 2013	◻ dry 2014	◻ dry 2015	◻ dry 2016
	◻ sdry 2014	◻ sdry 2015	

Figure 3.10.: Mean daily roughness length z_0 at Kaku tower as (a) boxplot over months and (b) as boxplot over functional seasons. The colors of the boxes in (a) depict the functional season in which the month mainly fell.

Figure 3.11.: Friction velocity against mean wind speed at Kaku tower for night time values (30-min data) (a) from the whole dataset and divided into the functional seasons (b) wet season, (c) transition period, and (d) dry season. Summer dry season was combined with dry season. Light grey to black colors of the dots show the density, with black being highest density.

3.3. Carbon fluxes

3.3.1. Net ecosystem exchange

Figure 3.12.: Cumulative (a) NEE, (b) GPP, and (c) R_{eco} over the functional seasons, divided into the four hydroecological years.

Table 3.2.: Cumulative NEE, GPP, R_{eco}, ET and Precipitation (P) over the whole hydrological year respectively.

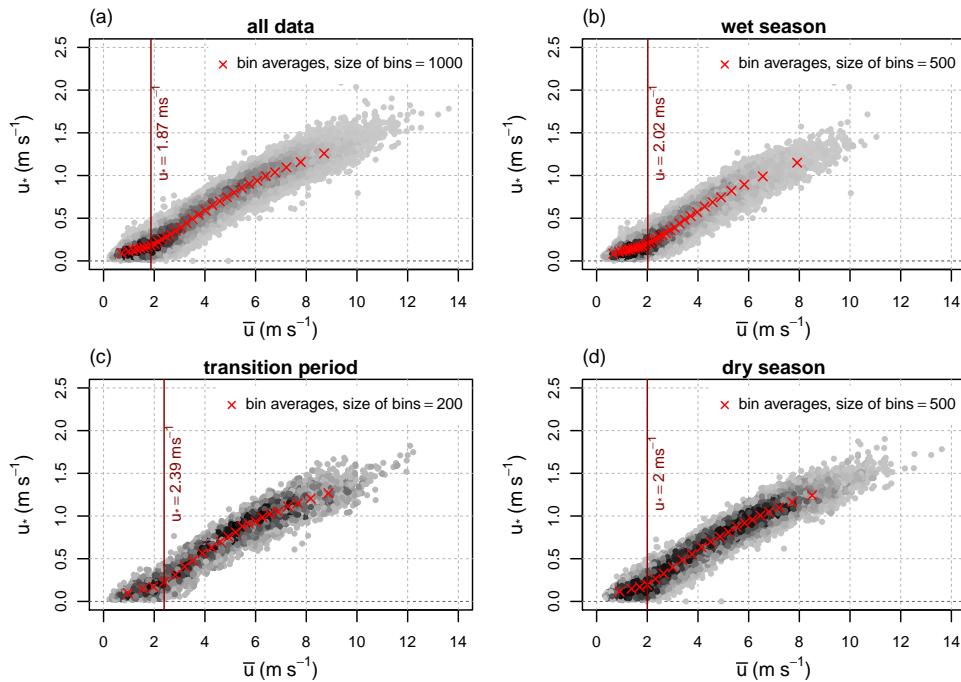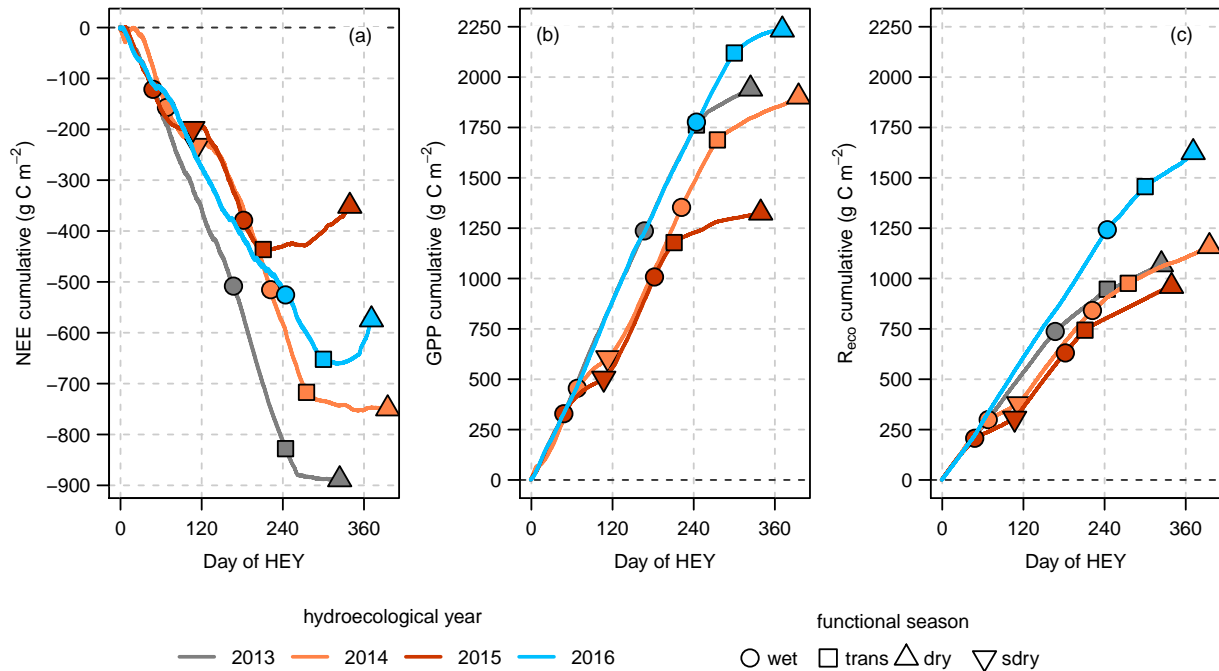| Year	NEE $(g_C\,m^{-2}\,yr^{-1})$	GPP $(g_C\,m^{-2}\,yr^{-1})$	R_{eco} $(g_C\,m^{-2}\,yr^{-1})$	ET $(mm\,yr^{-1})$	P $(mm\,yr^{-1})$
2013	−889	1942	1069	547	1270
2014	−749	1902	1160	570	1050
2015	−351	1326	962	476	541
2016	−574	2235	1626	905	1459

The courses of the cumulative carbon fluxes showed distinct differences for the four study years. The greatest annual net CO_2 uptake was observed in 2013, the year which was classified as ENSO-neutral (Fig. 3.12a and Tab. 3.2). In 2013 the slope of NEE was steepest and NEE decreased steadily until shortly after the end of the transition period at about day 260 of the hydroecological year. During the dry season NEE almost remained constant. The second largest net CO_2 sink was found for the year with a weak El Niño, 2014. The slope during wet season and transition period

was similar to that in the year 2013, but during the summer dry season a smaller slope was found. This led to an offset in NEE, visible in the difference between the cumulative sums at the end of the hydroecological years. In 2013 and 2014, NEE also remained almost constant during the dry season. The year 2016, classified as weak La Niña, showed the third highest net CO_2 uptake. Compared to the years 2013, 2014 and 2015, the slope during wet season and transition period was less steep. Furthermore, cumulative NEE not only stagnated but increased again during the dry season. The year 2015, classified as strong El Niño, showed the lowest net CO_2 uptake of only about a third of that in the year 2013. Wet season and transition period together were shorter than the wet season in 2014 which resulted in an early end of net CO_2 uptake. The dry season was by comparison long and also turned the ecosystem into a net source with increasing cumulative NEE.
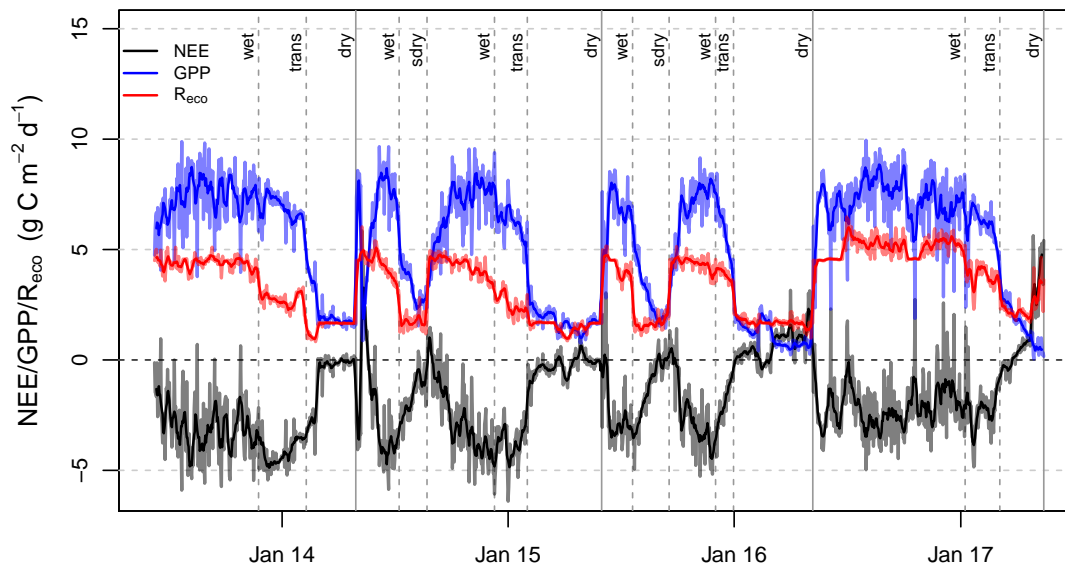
Figure 3.13.: Daily sums of NEE (black), GPP (blue) and R_{eco} (red) (light colored lines). 7-day running means are given as darker colored lines to emphasize the course. Vertical lines mark the end dates of the functional seasons (dashed lines) and additionally the end of the hydroecological year (solid lines).

3.3.2. Gross primary production

The highest annual CO_2 uptake with $2235\,\mathrm{g_C\,m^{-2}\,yr^{-1}}$ was observed in 2016, the year classified as weak La Niña (see Fig. 3.12b and Tab. 3.2). In the year classified as neutral, 2013, annual GPP was $293\,\mathrm{g_C\,m^{-2}\,yr^{-1}}$ less compared to 2016 due to a shorter wet season. Cumulative GPP in both 2016 and 2013 showed a steep and steady increase with similar slopes. The year 2014, weak El Niño, showed the third highest annual CO_2 uptake with only $40\,\mathrm{g_C\,m^{-2}\,yr^{-1}}$ less then in the year

Table 3.3.: Daily sums of NEE, GPP, R_{eco} and ET, means per functional season.

Functional season	NEE $(g_C\,m^{-2}\,d^{-1})$	GPP $(g_C\,m^{-2}\,d^{-1})$	R_{eco} $(g_C\,m^{-2}\,d^{-1})$	ET $(kg_{H_2O}\,m^{-2}\,d^{-1})$
2013				
wet season	−3.02	7.35	4.39	1.82
transition	−4.17	6.81	2.7	1.68
dry season	−0.71	2.2	1.53	1.4
2014				
wet season	−2.51	6.79	4.29	1.79
summer dry season	−1.61	3.27	1.7	0.84
transition	−3.76	6.25	2.53	1.56
dry season	−0.24	1.75	1.52	1.08
2015				
wet season	−2.47	6.76	4.3	1.89
summer dry season	−1.25	2.89	1.65	0.83
transition	−1.88	5.74	3.86	2.07
dry season	0.67	1.14	1.69	1.03
2016				
wet season	−2.15	7.25	5.07	2.46
transition	−2.23	6.06	3.79	3.11
dry season	1.18	1.56	2.39	1.8

2013. A slightly decreased CO_2 uptake, visible as a decreased slope of cumulative GPP, could be observed during the summer dry season. But the offset in cumulative GPP that arose from the dry conditions during the summer dry season compared to GPP in 2013 was almost compensated by the longer hydroecological year. The year with strong El Niño, 2015, showed a reduction of 41 % in annual GPP compared to 2016. The low annual GPP in 2015 was caused by a summer dry season and a very short wet season and transition period, the shortest ones during the study period (see tab. 2.1).

3.3.3. Ecosystem respiration

The greatest annual CO_2 release with $1626\,g_C\,m^{-2}\,yr^{-1}$ was found in 2016, the year classified as weak La Niňa (Fig. 3.12c and Tab. 3.2). The slope of cumulative R_{eco} during wet season, transition period and dry season was in 2016 greater than in all three other years. Annual sums of R_{eco} in the years 2013, 2014 and 2015 were with 1069, 1160 and $962\,g_C\,m^{-2}\,yr^{-1}$ respectively quite similar, being about two thirds of that from 2016. The differences resulted mainly from the different lengths of the functional seasons and the summer dry seasons in 2014 and 2015.

3.4. Controls on carbon fluxes

Changes in radiation, i.e. incoming shortwave radiation and photosynthetic active radiation, temperature, and water availability and demand, i.e. soil moisture and water vapor deficit, are the main drivers for short-term variability in the carbon fluxes NEE, GPP and R_{eco}. As the site is located in the tropics with high temperatures over the whole year, light and water availability were the main drivers for seasonal and annual differences. To investigate whether changes in incoming shortwave radiation or the available soil moisture have a greater impact on NEE, GPP and R_{eco}, light use efficiency and water use efficiency were analyzed.

3.4.1. Light use efficiency

Annual sums of incoming shortwave radiation did not differ much during the study period despite the great differences in annual precipitation (Fig. 3.14). The slopes of cumulative global radiation were only slightly smaller during the wet season and transition period of the year 2013 and slightly greater during the dry season of the year 2015. The differences in the annual sums mostly resulted from the different lengths of the HEY.

Mean daytime light use efficiencies were calculated with equation 2.15 and ranged between $0\,mol_C\,mol_{photon}^{-1}$ during dry seasons and $0.035\,mol_C\,mol_{photon}^{-1}$ during wet seasons (Fig. 3.15a). In 2016, the year with weak La Niña, mean daytime LUE during the wet season was not lower as during the wet season in the year 2013 although more overcast days would have been expected due to the increased precipitation (Tab. 3.4). Light use efficiency during the wet seasons was in 2014 and 2015 significantly lower then in 2013 and 2016 (Mann-Whitney U test, $p < .001$ for wet seasons 2014 and 2015 vs. wet season 2013 and 2016). This resulted mostly from the decreased GPP in the wet seasons of the years 2014 and 2015 (Figs. 3.15c and d).
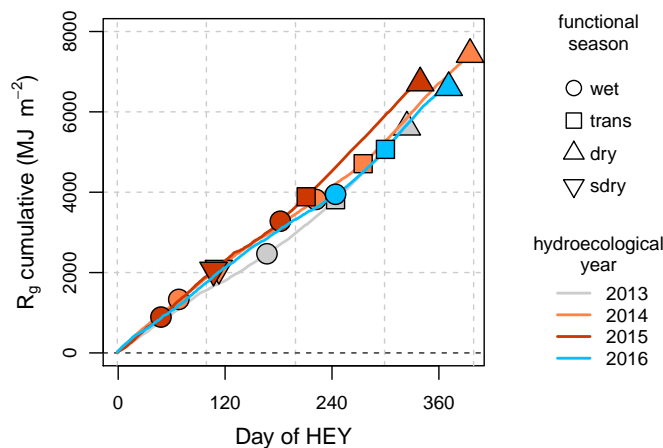

Figure 3.14.: Cumulative global radiation over the functional seasons, divided into the four hydroecological years. The symbols display the end of the functional season.
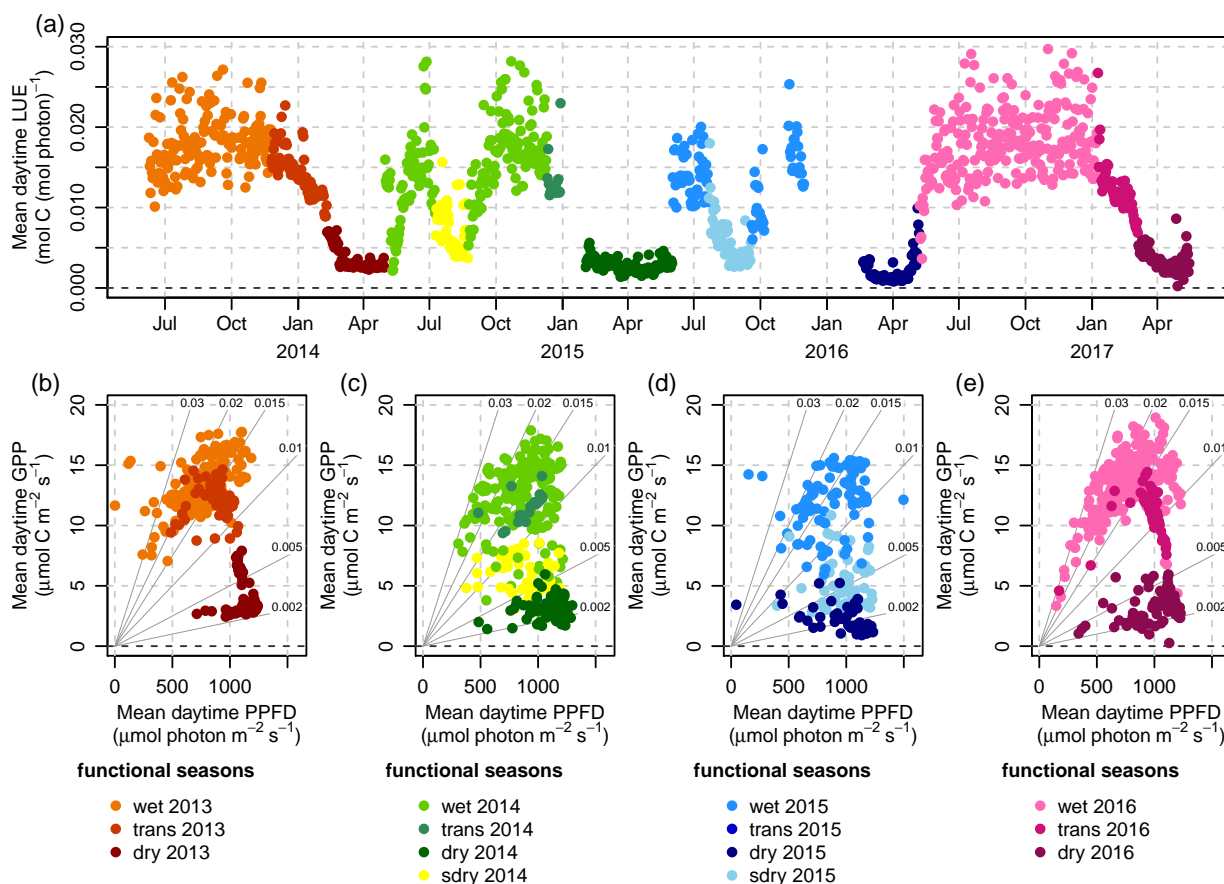
Figure 3.15.: Mean daytime light use efficiency (LUE) at Kaku tower as (a) time series for the study period and scatterplots of mean daytime GPP against mean daytime PPFD for the four hydroecological years (b) 2013, (c) 2014, (d) 2015, and (e) 2016. Slanted lines in (b), (c), (d), and (e) depict light use efficiency (LUE)

3.4.2. Water use efficiency

Mean daily water use efficiency was calculated with equation 2.11 and ranged between almost 0 and $24\,\mathrm{g_C\,kg_{H_2O}^{-1}}$ (Fig. 3.16a). WUE was highest in the wet season and transition period of the year 2013, which was classified as no ENSO event, with about $4.3\,\mathrm{g_C\,kg_{H_2O}^{-1}}$ (Tab. 3.4). In 2014, the year with weak El Niño, WUE was slightly lower with $4\,\mathrm{g_C\,kg_{H_2O}^{-1}}$ in wet season, summer dry season and transition period. In the year 2015, classified as strong El Niño, water use efficiency decreased from $3.8\,\mathrm{g_C\,kg_{H_2O}^{-1}}$ in the wet season to $2.8\,\mathrm{g_C\,kg_{H_2O}^{-1}}$ in the transition period. In the dry seasons, WUE was always significantly lower then in all other seasons (Mann-Whitney U test, p < .001 for all four years and versus all other seasons). In the year classified as weak La Niña, 2016, increased daily sums of ET on the one hand and no change in daily sums of GPP on the other hand led to significantly lower water use efficiencies in wet season, transition period and dry

37

season (Mann-Whitney U test, p < .001 for wet season, transition and dry season versus those of the other three years, except dry 2016 vs. dry 2015, which was only p < .005).

Table 3.4.: Water use efficiencies and light use efficiency at Kaku tower, means per functional season.

Functional season	WUE $(\mathrm{g_C\,kg_{H_2O}^{-1}})$	EWUE $(\mathrm{g_C\,kg_{H_2O}^{-1}})$	RWUE $(\mathrm{g_C\,kg_{H_2O}^{-1}})$	LUE $(\mathrm{mol_C\,mol_{photon}^{-1}})$
2013				
wet season	4.3	−1.7	2.6	0.018
transition	4.2	−2.6	1.6	0.014
dry season	1.7	−0.6	1.1	0.004
2014				
wet season	4	−1.5	2.6	0.015
summer dry season	4	−1.9	2.2	0.007
transition	4.1	−2.5	1.7	0.013
dry season	1.8	−0.2	1.6	0.003
2015				
wet season	3.8	−1.3	2.5	0.014
summer dry season	3.7	−1.4	2.3	0.006
transition	2.8	−0.9	1.9	NA[a]
dry season	1.2	0.7	1.8	0.002
2016				
wet season	3.2	−0.9	2.3	0.018
transition	2	−0.7	1.3	0.012
dry season	0.9	0.7	1.4	0.003

WUE = GPP/ET, EWUE = NEE/ET and RWUE = R$_{\mathrm{eco}}$/ET.
[a] NA = not available. Data gaps in PPFD spanned the entire transition period in 2015.

The relationship of water use efficiency gets much more linear and influences of seasonality are reduced when VPD is taken into account for the calculation. The parameter is then called inherent water use efficiency (IWUE) and is calculated with equation 2.12. This leads to a better comparability over the years. The ratios were similar for the years 2013, 2014 and 2015 with 30 to $33\,\mathrm{g_C\,hPa\,kg_{H_2O}^{-1}}$ (Figs. 3.16f to h). In 2016, the ratio was significantly lower with only $20\,\mathrm{g_C\,hPa\,kg_{H_2O}^{-1}}$ (Mann-Whitney U test, p-value < 0.001 for IWUE in 2016 compared to IWUE in 2013, 2014 and 2015 respectively) (Fig. 3.16i).

Mean daily ecosystem water use efficiency (EWUE) was calculated using equation 2.13. As daily mean sums of NEE were negative, indicating a net carbon sink, for almost the whole study period except for the dry seasons of 2015 and 2016, the daily mean EWUEs were negative for all seasons except dry seasons in 2015 and 2016, too (Tab. 3.4). EWUE showed highest rates of net carbon uptake per kg H$_2$O lost during the transition periods in 2013 and 2014, when respiration was already diminished but GPP still remained high (Figs. 3.17a to d).

Mean daily respiration water use efficiency (RWUE) was calculated with equation 2.14 and
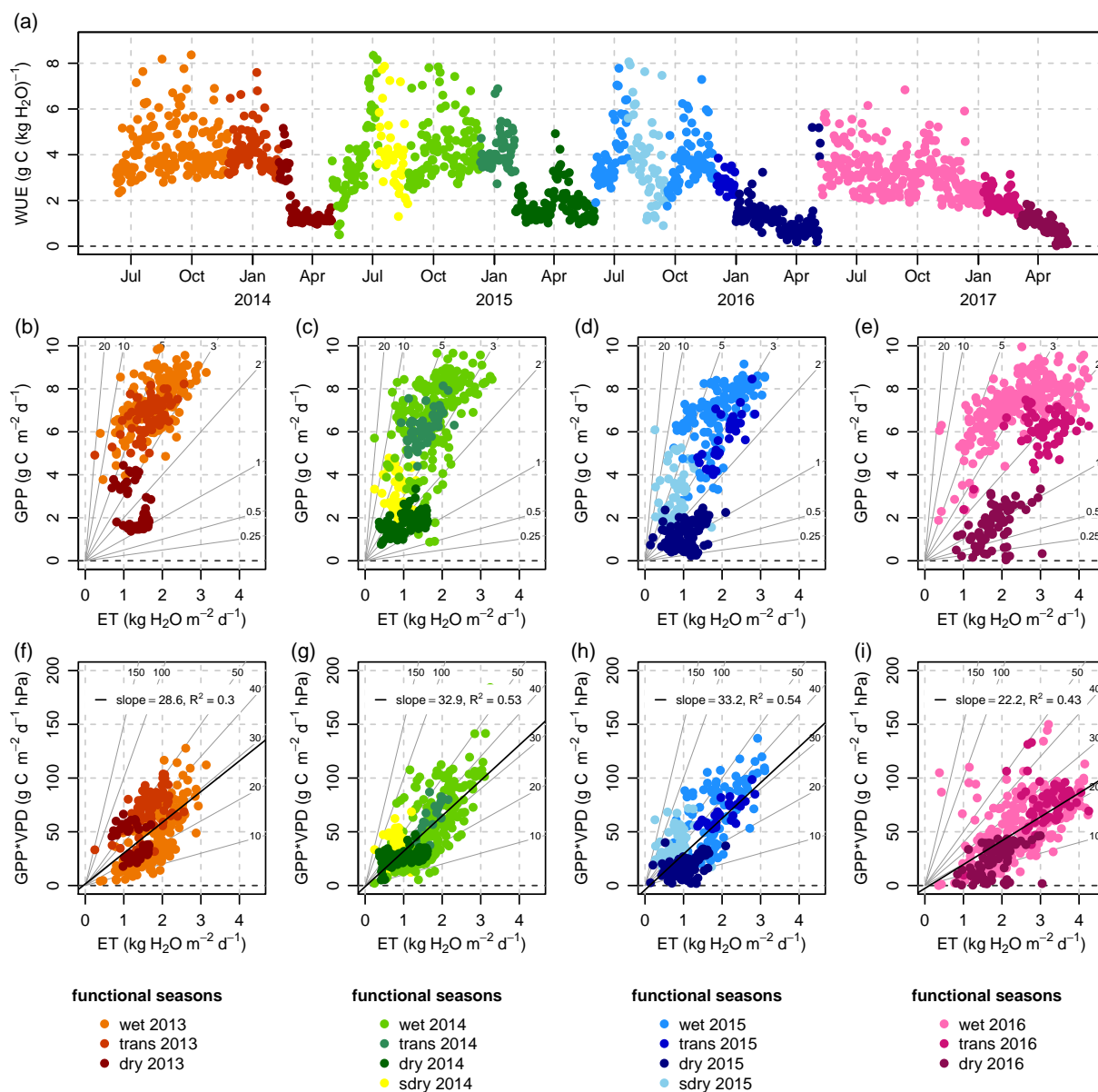
Figure 3.16.: Mean daily water use efficiency (WUE) at Kaku tower as (a) time series for the study period and scatterplots of mean daily sums of GPP against mean daily sums of ET for the four hydroecological years (b) 2013, (c) 2014, (d) 2015, and (e) 2016 and scatterplots of mean daily GPP*VPD against mean daily sums of ET for the four hydroecological years (f) 2013, (g) 2014, (h) 2015, and (i) 2016. Slanted lines in (b), (c), (d), and (e) depict water use efficiency (WUE). Slanted lines in (f), (g), (h), and (i) depict inherent water use efficiency (IWUE). The depicted WUE in (a) were limited to $10\,\mathrm{g_C\,kg_{H_2O}^{-1}}$. Only a few data points exceeded this range.

ranged between 0.5 and $20\,\mathrm{g_C\,kg_{H_2O}^{-1}}$ (compare slanted lines in Figs. 3.17e to h). RWUE was highest during wet seasons and decreased towards dry seasons (Tab. 3.4). In the scatterplots a clear differentiation between the different seasons was visible.

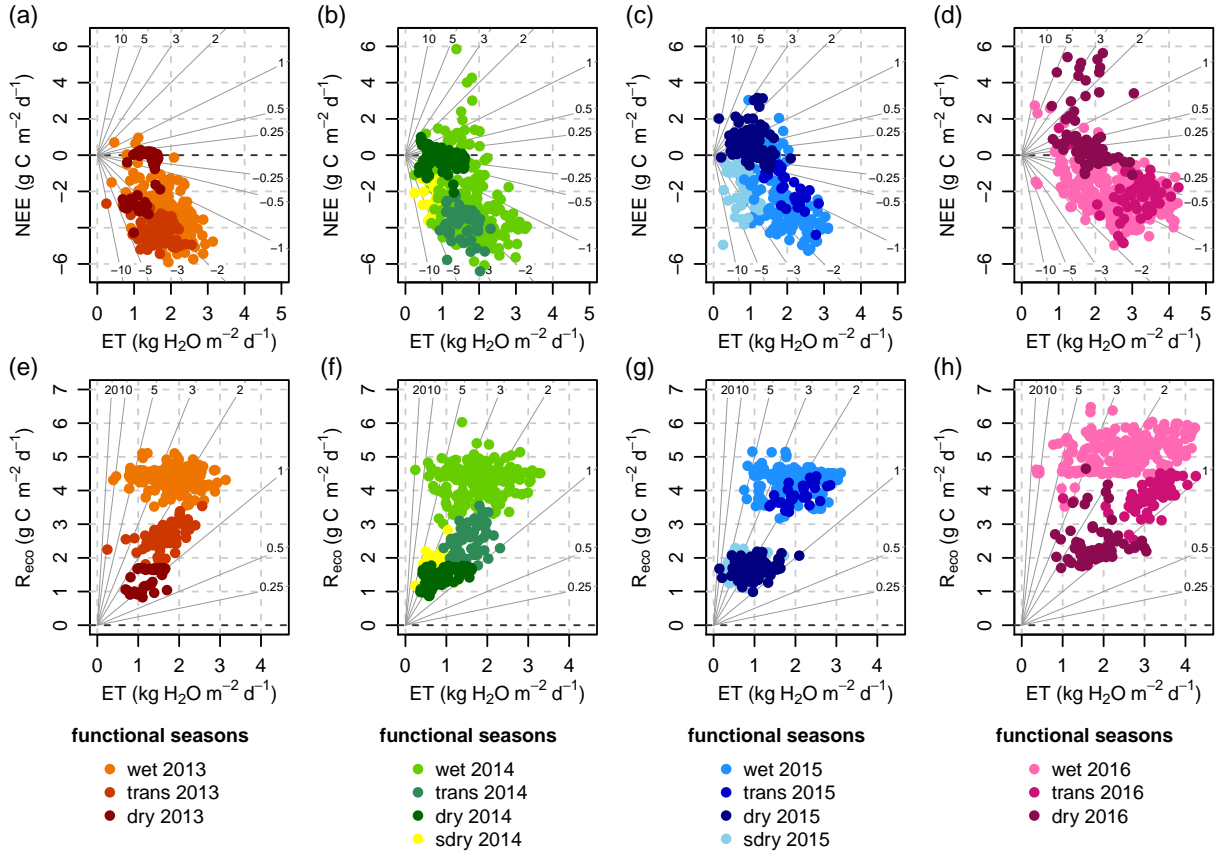**Figure 3.17.:** Scatterplots of mean daily sums of NEE against mean daily sums of ET for the four hydroecological years (a) 2013, (b) 2014, (c) 2015, and (d) 2016, and scatterplots of mean daily sums of R_{eco} against mean daily sums of ET for the four hydroecological years (e) 2013, (f) 2014, (g) 2015, and (h) 2016. Slanted lines depict ecosystem water use efficiency (EWUE) in (a), (b), (c), and (d) and respiration water use efficiency (RWUE) in (e), (f), (g), and (h) respectively.

4. Discussion

4.1. Quantification of carbon and energy fluxes

The first aim of this study was to quantify the carbon and energy fluxes and to analyze them for the individual functional seasons. For the carbon fluxes, the Hypothesis was that the ecosystem is a net sink during wet season and transition period and a net source during dry season and summer dry season. For the momentum flux, six different conceptional models were proposed in section 1.

4.1.1. Momentum flux

As the logarithmic wind profile yields a straight line when plotted in a semi-logarithmic plot with the natural logarithm of the height z on the y-axis and the mean wind speed u on the x-axis, the function equation can be written as:

$$ln(z) = \frac{\kappa}{u_*} \cdot u(z) + ln(z_0) \tag{4.1}$$

$$ln(z) = a \cdot u(z) + b$$

with a as slope $= \frac{\kappa}{u_*}$ and b as intersect $= ln(z_0)$.

Both z_0 and u_* were higher during the dry season than during the wet season (Fig. 3.10 and Fig. 3.11). Regarding z_0, this indicates that the dense leaf canopy developing during the wet season decreases the roughness of the surface, making it more smooth. During the dry season, the bare branches increase the roughness.

Considering the wind profile, as the slope a is the inverse of u_*, the slope is decreased during the dry season and increased during the wet season. With higher z_0 for the dry season than for the wet season, the logarithmic wind profile for wet and dry season would look like Figure 4.1. This seems also reasonable as the wind speeds in 30 m agl were also higher during the dry season than during the wet season (Fig. 3.3a).

4.1.2. Daily carbon fluxes

The study site in SRNP showed negative daily sums of NEE almost for every functional season throughout the study period. Only in the dry seasons of 2015 and 2016, mean daily sums of NEE
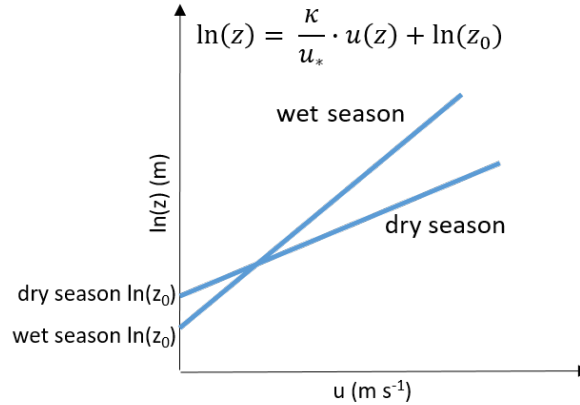
Figure 4.1.: Conceptional figure of the logarithmic wind profile.
The blue lines show logarithmic wind profiles with different intercepts (natural logarithm of roughness length z_0) and slopes (inverse of friction velocity) for dry and wet season.

were positive with 0.67 and $1.18\,\mathrm{g_C\,m^{-2}\,d^{-1}}$ respectively. In 2015, the positive NEE resulted from low daily GPP due to the very dry strong El Niño year. In 2016, despite the higher-than-average amount of precipitation, daily GPP was low but ecosystem respiration was increased visibly. Wet seasons and transition periods showed lower, more negative daily sums of NEE (means of -2.5 and $-3.25\,\mathrm{g_C\,m^{-2}\,d^{-1}}$ respectively), than dry seasons and summer dry seasons (means of 0.21 and $-1.41\,\mathrm{g_C\,m^{-2}\,d^{-1}}$ respectively).

Studies in an other tropical dry forest from Perez-Ruiz et al. (2010) and Verduzco et al. (2015), conducted on a site in Mexico which is influenced by the North American Monsoon System, found similar mean daily sums of NEE of about $0\,\mathrm{g_C\,m^{-2}\,d^{-1}}$ during the dry season and negative daily NEE of up to $-5\,\mathrm{g_C\,m^{-2}\,d^{-1}}$ during the monsoon season. But as the Mexican TDF lays at the lower end of the precipitation range for tropical dry forests with annual precipitation sums of 500 to 750 mm and a much shorter growing season, annual sums of NEE were noticeably less negative with up to $-153.1\,\mathrm{g_C\,m^{-2}\,yr^{-1}}$.

This pattern is different to findings from tropical rain forest sites with precipitation amounts of 1920, 2000 and 3041 mm respectively, where negative daily NEE were found mostly during the short dry seasons and positive daily NEE or daily NEE around zero during the wet season (Hutyra et al., 2007; Goulden et al., 2004; Bonal et al., 2008).

Other semiarid ecosystems showed high respiration rates and low GPP at the beginning of the wet season, when first soil water powered microbial decomposition of accumulated litter but most deciduous trees weren't fully green yet, leading to high positive daily means of NEE (Perez-Ruiz et al., 2010; Vourlitis et al., 2001). This phenomenon couldn't be observed at this site during the study period as for all three years, larger gaps which were filled with modeled data occurred directly before, during, or after the turn of the year. This caused abrupt changes in means of daily NEE, GPP and R_{eco} which occurred due to different modeling parameters for the different

functional seasons, and couldn't be attributed directly to vegetational changes.

4.1.3. Annual sums of carbon fluxes

High annual sums of NEE of -351 to $-889\,\mathrm{g_C\,m^{-2}\,yr^{-1}}$ where found for the study site. With a maximum annual sum of NEE of $-889\,\mathrm{g_C\,m^{-2}\,yr^{-1}}$, the tropical dry forest in SRNP belongs to the ecosystems with the strongest net C-sinks found in studies. Law et al. (2002) compared NEE per year from a considerable amount of study sites and few ecosystems showed similar or more negative yearly NEE than the SRNP site. Only some evergreen coniferous forests, for example in Scotland (Aberfeldy (AB), $-707\,\mathrm{g_C\,m^{-2}\,yr^{-1}}$ in 1997) and the USA (Duke, NC (DU), $-538\,\mathrm{g_C\,m^{-2}\,yr^{-1}}$ in 1998, $-651\,\mathrm{g_C\,m^{-2}\,yr^{-1}}$ in 1999) or deciduous broadleaf forests, for example in the USA (Walker Branch, TN (WB), $-470\,\mathrm{g_C\,m^{-2}\,yr^{-1}}$ in 1995 to $-870\,\mathrm{g_C\,m^{-2}\,yr^{-1}}$ in 1998) or in Belgium (Vielsam (VB), $-507\,\mathrm{g_C\,m^{-2}\,yr^{-1}}$ in 1998) showed similarly strong net C-sinks.

Partly, this finding can be attributed to the amount of precipitation that SRNP gets. Becknell et al. (2012) found increasing rates of biomass accumulation with increasing amounts of annual precipitation in tropical dry forests and SRNP lays with a mean of 1238.75 mm at the higher end of the precipitation range. Furthermore, forests of secondary succession show additionally increased rates of biomass accumulation, too (Goulden et al., 2004).

To answer the first research question, it can be said that the hypothesis was confirmed for the wet season. The ecosystem was a net carbon sink during the wet season and also during the transition period. Surprisingly, the ecosystem was also a net sink for most of the summer dry seasons and dry seasons. Only in particularly dry years (El Niño) and wet years (La Niña), the ecosystem turned into a net carbon source during the dry seasons.

4.2. Evaluation of ENSO influences

The second aim of this work was to analyze, how ENSO events alter the carbon fluxes. It was hypothesized that during La Niña years NEE is decreased, i.e. more negative, due to higher precipitation amounts which enhance GPP more than $\mathrm{R_{eco}}$. During El Niño years it was hypothesized that NEE is increased, i.e. less negative, due to lower precipitation amounts which diminish GPP.

4.2.1. Influences of ENSO on climate patterns

In Central America, the interannual variability of the climate can mainly be attributed to SST changes in the surrounding Oceans, with the main mechanism being the El Niño-Southern Oscillation (Giannini et al., 2001). Also in this study, the climate in the study region showed a clear connection to ENSO states. During El Niño years, precipitation was decreased by 19.2 % compared to years with neutral ENSO conditions. In La Niña years, precipitation was increased by 34.6 % and 65.3 % for weak and strong La Niña events, respectively. This corresponds well with findings

from Ropelewski and Halpert (1987) and Waylen et al. (1996), who reported decreased precipitation during summer in Central America and the northwestern part of Costa Rica. Similar effects on precipitation are predicted to occur due to climate change. Model simulations by Karmalkar et al. (2011) showed a decrease of about 25 % in precipitation, and an air temperature increase of 5.3 to 5.8 °C during the wet season and 3.7 to 4.2 °C during the dry season, along the western coast of Nicaragua, Costa Rica and Panama for 2070 to 2100, relative to modern-day values.

4.2.2. ENSO influencing carbon and energy fluxes

The year with neutral ENSO conditions, 2013, had with $-889\,\mathrm{g_C\,m^{-2}\,yr^{-1}}$ the lowest, most negative NEE during the study period.

In El Niño years, the existence of summer dry seasons and the length of the growing season (wet season plus transition period) mainly influenced the magnitude of the annual net C-sink. Although the rates of carbon uptake and carbon release were very similar within the wet season and transition period across all four hydroecological years, decreased daily rates of carbon uptake during the summer dry season led to a smaller slope of cumulative GPP, which caused a visual offset in the cumulative GPP in the years 2014 and 2015 compared to that in the years 2013 and 2016. In 2014, the annual sum of NEE was nevertheless only slightly less negative than in 2013, due to the long growing season, which was almost as long as the one from the year 2013 (231 d in 2014 compared to 245 d in 2013, see Tab. 2.1). In 2015, the growing season was with 153 d almost three months shorter than in 2013 with 42 % less precipitation than the average and additionally, daily rates of NEE were positive during the dry season, which led to the lowest net carbon uptake for the study period (Fig. 3.12).

In particularly wet years like the La Niña year 2016, with about 200 mm more precipitation, the annual net C-sink was not greater than in years with average rainfall but significantly smaller. Although daily rates of GPP were higher compared to 2015, they were not as high as during 2013. Daily rates of ecosystem respiration on the other hand were increased strongly compared to the other years, which led to less negative rates of daily NEE and the highest mean daily NEE during the dry season. The annual sum of ET was almost twice as high as in the other three years and daily rates of ET were increased by about $0.6\,\mathrm{kg_{H_2O}\,m^{-2}\,d^{-1}}$, but as GPP is increased only slightly, WUE is smallest for all seasons. LUE in contrast wasn't significantly different from the other years, indicating that increased cloud cover is not diminishing GPP in La Niña years. This indicates that the ecosystem is water-limited and not light-limited.

As annual precipitation could be reduced by about 25 % until 2100 as discussed in section 4.2.1, and the ecosystem is sensitive to a reduction in precipitation, the ecosystem is very vulnerable to climate change and the annual net C-uptake could decrease significantly.

For the second research question, the expectation was met for dry El Niño years, where annual NEE was less negative than during years with neutral ENSO conditions. For years with increased

precipitation, in contrast, the expectation was not met. In La Niña years, the annual NEE is also less negative due to increased respiration but almost unchanged GPP.

5. Conclusions

The aim of this study was to get a better understanding of the dynamics of energy and carbon fluxes in tropical dry forests. To achieve this, ecosystem-scale atmospheric flux estimates from the eddy covariance technique were analyzed for different functional seasons and for years with different ENSO phases.

The results showed that the ecosystem was a net carbon sink throughout the year, surprisingly even in dry seasons, which did not confirm the hypothesis. Only in very dry El Niño-years and in very wet La Niña-years, the ecosystem became a net carbon source during the dry season. During the La Niña-year, this was due to increased precipitation which enhanced respiration. In El Niño years, daily GPP was slightly decreased in contrast to R_{eco}, which led to the positive NEE during the dry season. In years with no ENSO event or only weak El Niño, daily rates of GPP and R_{eco} were very similar comparing the same seasons between the different years. Greatest net carbon sinks were also found during years with no ENSO event or weak El Niño. In strong El Niño years, the net carbon sink was decreased due to diminished GPP which confirmed the hypothesis, but contrasting to the proposed hypothesis, wet La Niña years also showed a decreased magnitude of net carbon sink due to higher ecosystem respiration.

Thus, four points are most crucial for the annual net carbon balance:

1. The length of the growing season (wet season + transition period)

2. The existence of a summer dry season

3. If extraordinary amounts of precipitation due to La Niña events enhance R_{eco}

4. If particularly dry El Niño years decrease GPP.

Considering the methodology, investigating other gap filling methods would be In the approach used in this thesis, the function for modeling respiration only depends on temperature. Regarding the small range of temperatures, testing different models that not only depend on temperature would increase the precision of the modeled respiration.

The study indicates that the ecosystem could react very vulnerably to decreasing amounts of precipitation due to a changing climate. Further research could increase the knowledge about this connection. For future research, further studies in tropical dry forests with similar amounts of precipitation would also be most valuable. The tropical dry forest in Santa Rosa National

Park in Costa Rica showed surprisingly high annual net uptake of carbon dioxide and it would be interesting to see if comparable ecosystems show similar rates of CO_2 uptake.

Acknowledgements

Declaration of Authorship

I hereby declare that the thesis titled "Carbon and Energy Exchange in a Tropical Dry Forest in Costa Rica with regard to El Niño-Southern Oscillation Dynamics" is my own unaided work. All direct or indirect sources used are acknowledged as references. This paper was not previously submitted for the attainment of any other academic degree and has not been published.

Ich erkläre hiermit, dass ich die Masterarbeit mit dem Titel "Carbon and Energy Exchange in a Tropical Dry Forest in Costa Rica with regard to El Niño-Southern Oscillation Dynamics" ohne fremde Unterstützung verfasst habe. Alle von mir genutzten Quellen und Hilfsmittel sind in den Quellenangaben angegeben. Die Arbeit wurde nicht bereits zur Erlangung eines akademischen Grades eingereicht und nicht veröffentlicht.

Bayreuth, January 27, 2020   Elena Loos

_____

Bibliography

Adler, D. and Kelly, S. T.: vioplot: violin plot, URL `https://github.com/TomKellyGenetics/vioplot`, r package version 0.3.0, 2018.

Ahlström, A., Raupach, M. R., Schurgers, G., Smith, B., Arneth, A., Jung, M., Reichstein, M., Canadell, J. G., Friedlingstein, P., Jain, A. K., Kato, E., Poulter, B., Sitch, S., Stocker, B. D., Viovy, N., Wang, Y. P., Wiltshire, A., Zaehle, S., and Zeng, N.: The dominant role of semi-arid ecosystems in the trend and variability of the land CO2 sink, Science, 348, 895–899, 2015.

AppEEARS Team: Application for Extracting and Exploring Analysis Ready Samples (AppEEARS). Ver. 2.18.1, NASA EOSDIS Land Processes Distributed Active Archive Center (LP DAAC), USGS/Earth Resources Observation and Science (EROS) Center, Sioux Falls, USA, URL `https://www.lpdaacsvc.cr.usgs.gov/appeears/`, accessed: 2019-04-18, 2019.

Becknell, J. M., Kucek, L. K., and Powers, J. S.: Aboveground biomass in mature and secondary seasonally dry tropical forests: A literature review and global synthesis, Forest Ecology and Management, 276, 88 – 95, 2012.

Beer, C., Ciais, P., Reichstein, M., Baldocchi, D., Law, B. E., Papale, D., Soussana, J.-F., Ammann, C., Buchmann, N., Frank, D., Gianelle, D., Janssens, I. A., Knohl, A., Köstner, B., Moors, E., Roupsard, O., Verbeeck, H., Vesala, T., Williams, C. A., and Wohlfahrt, G.: Temporal and among-site variability of inherent water use efficiency at the ecosystem level, Global Biogeochemical Cycles, 23, 2009.

Beer, C., Reichstein, M., Tomelleri, E., Ciais, P., Jung, M., Carvalhais, N., Rödenbeck, C., Arain, M. A., Baldocchi, D., Bonan, G. B., Bondeau, A., Cescatti, A., Lasslop, G., Lindroth, A., Lomas, M., Luyssaert, S., Margolis, H., Oleson, K. W., Roupsard, O., Veenendaal, E., Viovy, N., Williams, C., Woodward, F. I., and Papale, D.: Terrestrial Gross Carbon Dioxide Uptake: Global Distribution and Covariation with Climate, Science, 329, 834–838, 2010.

Bonal, D., Bosc, A., Ponton, S., Goret, J.-Y., Burban, B., Gross, P., Bonnefond, J.-M., Elbers, J., Longdoz, B., Epron, D., Guehl, J.-M., and Granier, A.: Impact of severe dry season on net ecosystem exchange in the Neotropical rainforest of French Guiana, Global Change Biology, 14, 1917–1933, 2008.

Brown, S. and Lugo, A. E.: The Storage and Production of Organic Matter in Tropical Forests and Their Role in the Global Carbon Cycle, Biotropica, 14, 161–187, 1982.

Bulmer, M. G.: Principles of statistics, Courier Corporation, 1979.

Cane, M. A. and Zebiak, S. E.: A Theory for El Niño and the Southern Oscillation, Science, 228, 1085–1087, 1985.

Castro, S. M., Sanchez-Azofeifa, G. A., and Sato, H.: Effect of drought on productivity in a Costa Rican tropical dry forest, Environmental Research Letters, 13, 045 001, 2018.

Daubenmire, R.: Phenology and other characteristics of tropical semi-deciduous forest in northwestern Costa Rica, The Journal of Ecology, pp. 147–170, 1972.

Ewel, J. J.: Natural systems as models for the design of sustainable systems of land use, Agroforestry Systems, 45, 1–21, 1999.

FAO: Global Forest Resources Assessment 2015. How are the World's Forests Changing?, UN Food and Agriculture Organization, Rome, second edn., 2015.

Foken, T. and Wichura, B.: Tools for quality assessment of surface-based flux measurements, Agricultural and Forest Meteorology, 78, 83–105, 1996.

Foken, T., Göckede, M., Mauder, M., Mahrt, L., Amiro, B. D., and Munger, J. W.: Handbook of Micrometeorology: A Guide for Surface Flux Measurements, chap. Post-field data quality control, pp. 181–208, Kluwer Acad., Dordrecht, Netherlands, 2004.

Frankie, G. W., Baker, H. G., and Opler, P. A.: Comparative Phenological Studies of Trees in Tropical Wet and Dry Forests in the Lowlands of Costa Rica, Journal of Ecology, 62, 881–919, 1974.

Giannini, A., Kushnir, Y., and Cane, M. A.: Seasonality in the impact of ENSO and the north atlantic high on caribbean rainfall, Physics and Chemistry of the Earth, Part B: Hydrology, Oceans and Atmosphere, 26, 143 – 147, 2001.

Goulden, M. L., Miller, S. D., da Rocha, H. R., Menton, M. C., de Freitas, H. C., e Silva Figueira, A. M., and de Sousa, C. A. D.: Diel and Seasonal Patterns of Tropical Forest CO_2 Exchange, Ecological Applications, 14, 42–54, 2004.

Hanley, D. E., Bourassa, M. A., O'Brien, J. J., Smith, S. R., and Spade, E. R.: A quantitative evaluation of ENSO indices, Journal of Climate, 16, 1249–1258, 2003.

Hinko-Najera, N., Isaac, P., Beringer, J., van Gorsel, E., Ewenz, C., McHugh, I., Exbrayat, J.-F., Livesley, S. J., and Arndt, S. K.: Net ecosystem carbon exchange of a dry temperate eucalypt forest, Biogeosciences, 14, 3781, 2017.

Hoekstra, J. M., Boucher, T. M., Ricketts, T. H., and Roberts, C.: Confronting a biome crisis: global disparities of habitat loss and protection, Ecology letters, 8, 23–29, 2005.

Holdridge, L. R.: Life zone ecology., (rev. ed.), Tropical Science Center, San Jose, Costa Rica, 1967.

Hollinger, D. Y. and Richardson, A. D.: Uncertainty in eddy covariance measurements and its application to physiological models, Tree Physiology, 25, 873–885, 2005.

Huang, L., He, B., Chen, A., Wang, H., Liu, J., Lü, A., and Chen, Z.: Drought dominates the interannual variability in global terrestrial net primary production by controlling semi-arid ecosystems, Scientific reports, 6, 24 639, 2016.

Hubbell, S. P.: Tree Dispersion, Abundance, and Diversity in a Tropical Dry Forest, Science, 203, 1299–1309, 1979.

Hutyra, L. R., Munger, J. W., Saleska, S. R., Gottlieb, E., Daube, B. C., Dunn, A. L., Amaral, D. F., de Camargo, P. B., and Wofsy, S. C.: Seasonal controls on the exchange of carbon and water in an Amazonian rain forest, Journal of Geophysical Research: Biogeosciences, 112, 2007.

Janzen, D. H.: Guanacaste National Park: tropical ecological and cultural restoration, Rehabilitating damaged ecosystems, 1986.

Janzen, D. H.: Caterpillar seasonality in a Costa Rican dry forest, Caterpillars. Ecological and evolutionary constraints on foraging., 1993.

Karmalkar, A. V., Bradley, R. S., and Diaz, H. F.: Climate change in Central America and Mexico: regional climate model validation and climate change projections, Climate Dynamics, 37, 605, 2011.

Keenan, R. J., Reams, G. A., Achard, F., de Freitas, J. V., Grainger, A., and Lindquist, E.: Dynamics of global forest area: Results from the FAO Global Forest Resources Assessment 2015, Forest Ecology and Management, 352, 9–20, changes in Global Forest Resources from 1990 to 2015, 2015.

Law, B. E., Falge, E., Gu, L., Baldocchi, D. D., Bakwin, P., Berbigier, P., Davis, K., Dolman, A. J., Falk, M., Fuentes, J. D., Goldstein, A., Granier, A., Grelle, A., Hollinger, D., Janssens, I. A., Jarvis, P., Jensen, N. O., Katul, G., Mahli, Y., Matteucci, G., Meyers, T., Monson, R., Munger, W., Oechel, W., Olson, R., Pilegaard, K., U, K. T. P., Thorgeirsson, H., Valentini, R., Verma, S., Vesala, T., Wilson, K., and Wofsy, S.: Environmental controls over carbon dioxide and water vapor exchange of terrestrial vegetation, Agricultural and Forest Meteorology, 113, 97 – 120, fLUXNET 2000 Synthesis, 2002.

Lemon, J.: Plotrix: a package in the red light district of R, R-News, 6, 8–12, 2006.

Liu, H., Peters, G., and Foken, T.: New Equations For Sonic Temperature Variance And Buoyancy Heat Flux With An Omnidirectional Sonic Anemometer, Boundary-Layer Meteorology, 100, 459–468, 2001.

Lloyd, J. and Taylor, J. A.: On the Temperature Dependence of Soil Respiration, Functional Ecology, 8, 315, 1994.

Lyon, B. and Barnston, A. G.: ENSO and the Spatial Extent of Interannual Precipitation Extremes in Tropical Land Areas, Journal of Climate, 18, 5095–5109, 2005.

Lyra, A., Imbach, P., Rodriguez, D., Chou, S. C., Georgiou, S., and Garofolo, L.: Projections of climate change impacts on central America tropical rainforest, Climatic Change, 141, 93–105, 2017.

Malhi, Y., Baldocchi, D. D., and Jarvis, P. G.: The carbon balance of tropical, temperate and boreal forests, Plant, Cell & Environment, 22, 715–740, 1999.

McHugh, I. D., Beringer, J., Cunningham, S. C., Baker, P. J., Cavagnaro, T. R., Mac Nally, R., and Thompson, R. M.: Interactions between nocturnal turbulent flux, storage and advection at an "ideal" eucalypt woodland site, Biogeosciences, 14, 3027–3050, 2017.

Michaelis, L. and Menten, M. L.: Die Kinetik der Invertinwirkung, Biochemische Zeitschrift, 49, 333–369, 1913.

Miles, L., Newton, A. C., DeFries, R. S., Ravilious, C., May, I., Blyth, S., Kapos, V., and Gordon, J. E.: A global overview of the conservation status of tropical dry forests, Journal of Biogeography, 33, 491–505, 2006.

Monin, A. S. and Obukhov, A. M.: Osnovnye zakonomernosti turbulentnogo peremesivanija v prizemnom sloe atmosfery (Basic Laws of Turbulent Mixing in the Atmosphere Near the Ground), Trudy geofiz. inst. AN SSSR, 24, 163–187, 1954.

Moore, C.: Frequency response corrections for eddy correlation systems, Boundary-Layer Meteorology, 37, 17–35, 1986.

Obukhov, A.: Turbulentnost'v temperaturnoj-neodnorodnoj atmosfere (Turbulence in an Atmosphere with a Non-uniform Temperature), Trudy Inst. Theor. Geofiz. AN SSSR, 1, 95–115, 1946.

Olson, D. M., Dinerstein, E., Wikramanayake, E. D., Burgess, N. D., Powell, G. V., Underwood, E. C., D'amico, J. A., Itoua, I., Strand, H. E., Morrison, J. C., et al.: Terrestrial Ecoregions of the World: A New Map of Life on EarthA new global map of terrestrial ecoregions provides an innovative tool for conserving biodiversity, BioScience, 51, 933–938, 2001.

Pan, Y., Birdsey, R. A., Fang, J., Houghton, R., Kauppi, P. E., Kurz, W. A., Phillips, O. L., Shvidenko, A., Lewis, S. L., Canadell, J. G., Ciais, P., Jackson, R. B., Pacala, S. W., McGuire, A. D., Piao, S., Rautiainen, A., Sitch, S., and Hayes, D.: A Large and Persistent Carbon Sink in the World's Forests, Science, 333, 988–993, 2011.

Pan, Y., Birdsey, R. A., Phillips, O. L., and Jackson, R. B.: The Structure, Distribution, and Biomass of the World's Forests, Annual Review of Ecology, Evolution, and Systematics, 44, 593–622, 2013.

Perez-Ruiz, E. R., Garatuza-Payan, J., Watts, C. J., Rodriguez, J. C., Yepez, E. A., and Scott, R. L.: Carbon dioxide and water vapour exchange in a tropical dry forest as influenced by the North American Monsoon System (NAMS), Journal of Arid Environments, 74, 556 – 563, land Surface Ecohydrology of the North American Monsoon System, 2010.

Portillo-Quintero, C. and Sánchez-Azofeifa, G. A.: Extent and conservation of tropical dry forests in the Americas, Biological conservation, 143, 144–155, 2009.

Portillo-Quintero, C., Sanchez-Azofeifa, A., Calvo-Alvarado, J., Quesada, M., and do Espirito Santo, M. M.: The role of tropical dry forests for biodiversity, carbon and water conservation in the neotropics: lessons learned and opportunities for its sustainable management, Regional Environmental Change, 15, 1039–1049, 2015.

Poulter, B., Frank, D., Ciais, P., Myneni, R. B., Andela, N., Bi, J., Broquet, G., Canadell, J. G., Chevallier, F., Liu, Y. Y., Running, S. W., Sitch, S., and van der Werf, G. R.: Contribution of semi-arid ecosystems to interannual variability of the global carbon cycle, Nature, 509, 600, 2014.

Priestley, C. H. B. and Taylor, R. J.: On the Assessment of Surface Heat Flux and Evaporation Using Large-Scale Parameters, Monthly Weather Review, 100, 81–92, 1972.

R Core Team: R: A Language and Environment for Statistical Computing, R Foundation for Statistical Computing, Vienna, Austria, URL `https://www.R-project.org/`, 2018.

Reichstein, M., Tenhunen, J. D., Roupsard, O., Ourcival, J.-M., Rambal, S., Dore, S., and Valentini, R.: Ecosystem respiration in two Mediterranean evergreen Holm Oak forests: drought effects and decomposition dynamics, Functional Ecology, 16, 27–39, 2002.

Richardson, A. D., Hollinger, D. Y., Burba, G. G., Davis, K. J., Flanagan, L. B., Katul, G. G., Munger, J. W., Ricciuto, D. M., Stoy, P. C., Suyker, A. E., Verma, S. B., and Wofsy, S. C.: A multi-site analysis of random error in tower-based measurements of carbon and energy fluxes, Agricultural and Forest Meteorology, 136, 1 – 18, 2006.

Ropelewski, C. F. and Halpert, M. S.: Global and regional scale precipitation patterns associated with the El Niño/Southern Oscillation, Monthly weather review, 115, 1606–1626, 1987.

Sánchez-Azofeifa, G. A., Quesada, M., Rodríguez, J. P., Nassar, J. M., Stoner, K. E., Castillo, A., Garvin, T., Zent, E. L., Calvo-Alvarado, J. C., Kalacska, M. E., et al.: Research priorities for Neotropical dry forests, Biotropica: The Journal of Biology and Conservation, 37, 477–485, 2005.

Sanford, Jr., R. L., Paaby, P., Luvall, J. C., and Phillis, E.: La Selva: Ecology and Natural History of a Neotropical Rain Forest, chap. Climate, Geomorphology and Aquatic Systems, pp. 19–33, University of Chicago Press, Chicago, IL, 1994.

Schotanus, P., Nieuwstadt, F., and De Bruin, H.: Temperature measurement with a sonic anemometer and its application to heat and moisture fluxes, Boundary-Layer Meteorology, 26, 81–93, 1983.

Scott, R. L., Huxman, T. E., Cable, W. L., and Emmerich, W. E.: Partitioning of evapotranspiration and its relation to carbon dioxide exchange in a Chihuahuan Desert shrubland, Hydrological Processes, 20, 3227–3243, 2006.

Shuttleworth, W. J.: Terrestrial Hydrometeorology, John Wiley and Sons Ltd, 2012.

Thomas, C. and Foken, T.: Re-evaluation of integral turbulence characteristics and their parameterizations, 15th Conference on Turbulence and Boundary Layers, pp. 129–132, 2002.

Thomas, C., Wichura, B., and Foken, T.: Integrale Turbulenzcharakteristiken - ein Überblick, in: Österreichische Beiträge Zu Meteorologie Und Geophysik, vol. 27, p. 223, 2001.

Thomas, C. K., Law, B. E., Irvine, J., Martin, J. G., Pettijohn, J. C., and Davis, K. J.: Seasonal hydrology explains interannual and seasonal variation in carbon and water exchange in a semiarid mature ponderosa pine forest in central Oregon, Journal of Geophysical Research, 114, 2009.

Tosi, Jr., J. A. and Voertman, R. F.: Some Environmental Factors in the Economic Development of the Tropics, Economic Geography, 40, 189–205, 1964.

Trenberth, K. E.: The definition of el nino, Bulletin of the American Meteorological Society, 78, 2771–2778, 1997.

Verduzco, V. S., Garatuza-Payán, J., Yépez, E. A., Watts, C. J., Rodríguez, J. C., Robles-Morua, A., and Vivoni, E. R.: Variations of net ecosystem production due to seasonal precipitation differences in a tropical dry forest of northwest Mexico, Journal of Geophysical Research: Biogeosciences, 120, 2081–2094, 2015.

Vermote, E.: MOD09A1 MODIS/Terra Surface Reflectance 8-Day L3 Global 500m SIN Grid V006, NASA EOSDIS Land Processes DAAC, https://doi.org/10.5067/modis/mod09a1.006, 2015.

Vickers, D. and Mahrt, L.: Quality control and flux sampling problems for tower and aircraft data, Journal of Atmospheric and Oceanic Technology, 14, 512–526, 1997.

Vourlitis, G. L., Priante Filho, N., Hayashi, M. M. S., Nogueira, J. D. S., Caseiro, F. T., and Holanda Campelo Jr, J.: Seasonal variations in the net ecosystem CO_2 exchange of a mature Amazonian transitional tropical forest (cerradão), Functional Ecology, 15, 388–395, 2001.

Waylen, P. R., Caviedes, C. N., and Quesada, M. E.: Interannual Variability of Monthly Precipitation in Costa Rica, Journal of Climate, 9, 2606–2613, 1996.

Wilczak, J. M., Oncley, S. P., and Stage, S. A.: Sonic Anemometer Tilt Correction Algorithms, Boundary-Layer Meteorology, 99, 127–150, 2001.

Zeileis, A. and Grothendieck, G.: zoo: S3 Infrastructure for Regular and Irregular Time Series, Journal of Statistical Software, 14, 1–27, https://doi.org/10.18637/jss.v014.i06, 2005.

A. Definition of temperature classes

Gaps in NEE and ET were filled using different fit functions, as described in section 2.3.4, for different temperature classes. Five temperature classes were defined for each season, below 20th percentile, between 20th, 40th, 60th and 80th percentiles and above 80th percentile.
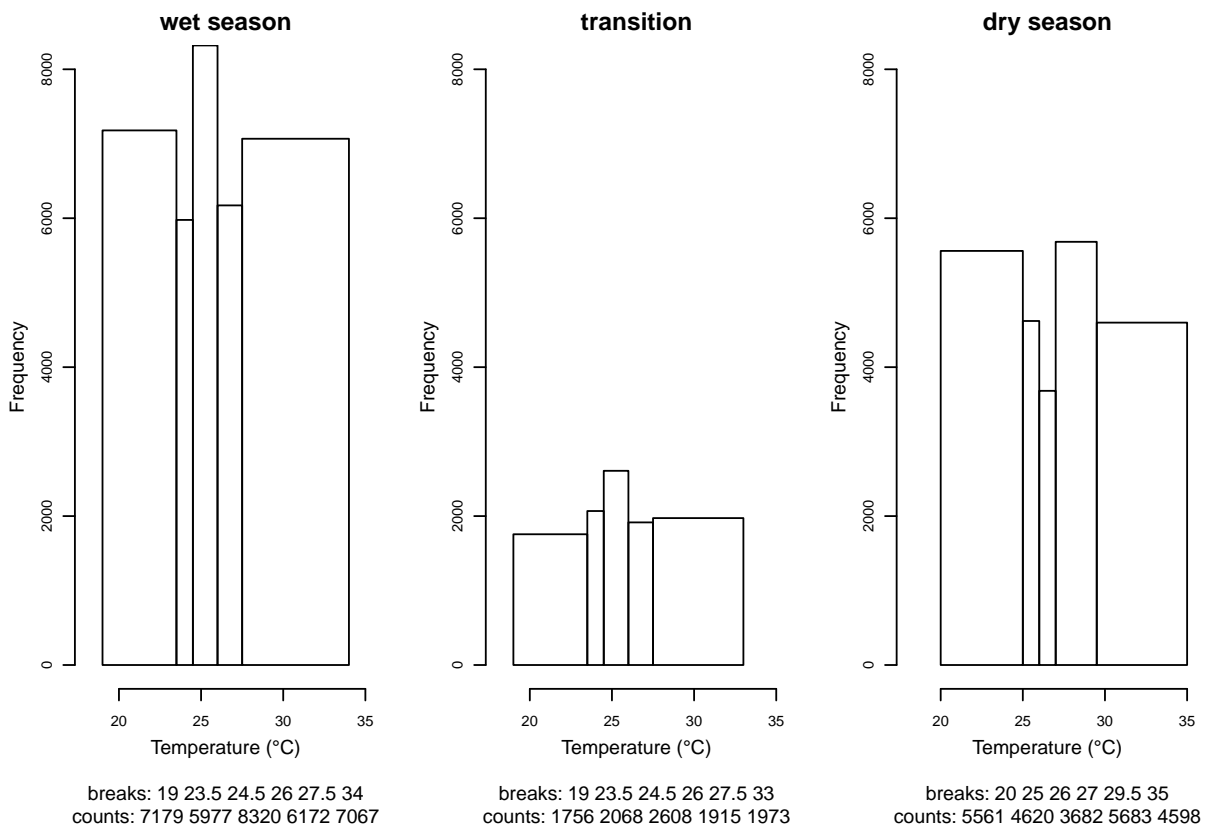

Figure A.1.: Definition of temperature classes for NEE and ET gap filling. Temperatures are from Kaku tower.
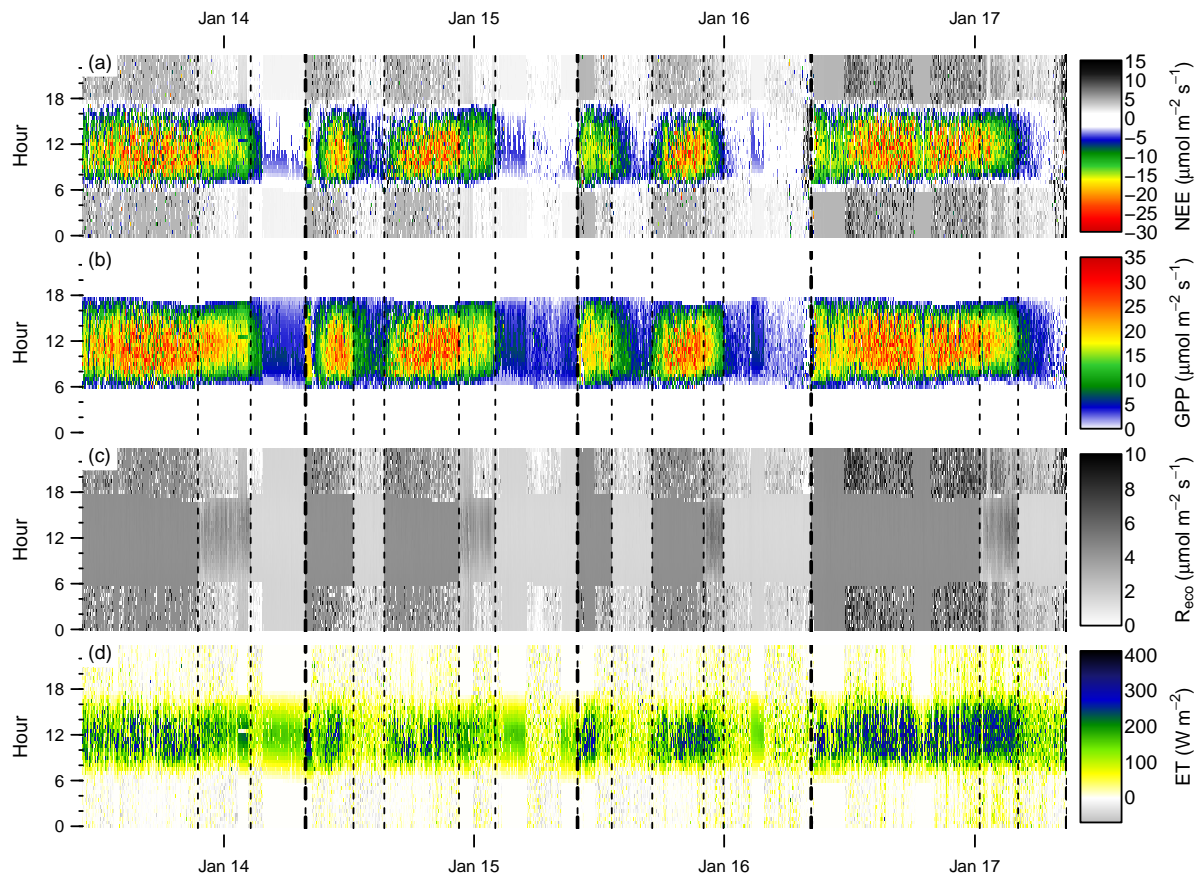
B. Hovmöller plot

Figure B.1.: Hovmöller plots for (a) NEE, (b) GPP, (c) R_{eco}, and (d) ET for Kaku tower. Vertical dashed lines mark the end dates of the functional seasons (thin dashed lines) and additionally the end of the hydroecological year (thicker dashed lines).